JOURNAL OF COMPUTATIONAL PHYSICS 95, 117–166 (1991)

Self-Consistent Numerical "Bounce-Averaged" Transport Computations in Stellarators Employing a Multi-mesh Approach

W. D. D'HAESELEER*, W. N. G. HITCHON, AND J. L. SHOHET

Torsatron/Stellarator Laboratory, University of Wisconsin-Madison, Madison, Wisconsin 53706

Received August 3, 1989; revised March 9, 1990

A numerical code FLOCS (flow code for stellarators), allowing a self-consistent computation of neoclassical stellarator transport, has been developed. Starting from a bounce-averaged kinetic equation, the distribution function $\langle f \rangle$ is found as a function of one spatial variable (poloidal angle) and two velocity-space variables (energy and a pitch-angle (pa) variable). Special care is needed at the phase-space boundary where particles can entrap (detrap) collisionlessly into (out of) a helical ripple. The natural choice for the pa variable is therefore the ripple-depth parameter y being 1 at the trapping boundary, approaching 0 for very deeply trapped particles, and going to ∞ for very passing particles. Since $\langle f \rangle$ is to contain information from which, in addition to the radial fluxes (and thus the confinement times and the ambipolar electric field), the parallel flows and currents should be computable, the entire velocity space must be covered, including very large y values. Numerical stability arguments in combination with CPU-time considerations, on the one hand, versus the physical behavior of $\langle f \rangle$ for very large y values, on the other hand, suggested the use of a multi-mesh approach (in the variable y) up to a reasonable value of $y \sim 100$. FLOCS extends the range of validity of a previously developed bounce-averaged code FPSTEL. After presenting some issues concerning FPSTEL, which are of relevance to our approach, the code FLOCS is described in detail, and some initial results on the distribution function are given.

I. INTRODUCTION

Stellarators are a serious alternative to the main tokamak line in magnetic fusion, partly because anomalous losses seem to be smaller than in tokamaks, presumably because of the absence of a large inductively generated current in stellarators.

Neoclassical transport, being the transport caused by magnetic-field inhomogeneities, thus seems to be relatively more important in stellarators than in tokamaks.

* Present address: The NET Team, Max-Planck-Institut für Plasmaphysik, D-8046 Garching-bei-Muenchen, Germany.

0003-4916/91 $7.50

In addition to confinement time and radial fluxes, it is imperative to investigate a different prediction of neoclassical theory: the existence of a parallel current proportional to the pressure gradient, known as the *bootstrap* (bs) current.

In stellarators, this parallel current could be disadvantageous because it could jeopardize equilibrium and/or stability. On the other hand, it could turn out to be a blessing rather than a curse, in that it might help to provide additional rotational transform in low aspect-ratio stellarators, in which it could be difficult to obtain the required rotational transform solely from external currents flowing in helical windings or modular coils. Once the bs current is known in stellarators, the importance of anomalous losses should be reconsidered.

These are some of the reasons why the study of neoclassical transport in stellarators needs attention. In the present work we have developed a self-consistent numerical computation of stellarator neoclassical transport.

Although useful analytic treatments exist, they have concentrated on asymptotic regimes, and used other simplifications. Interaction between species is usually neglected. Even the recently developed moment-equation approach [1, 2] has been used in ways which suffer from many of the assumptions usually made in analytic kinetic theory. The same can be said about numerical computations undertaken previously. Although they undoubtedly add to the mosaic of different viewpoints, they also suffer from some shortcomings. As will be discussed below, in some of that work, certain physical processes had to be ignored for computational purposes (which, although presenting a problem for describing the correct particle trajectories, do not seem to affect the transport results, however—at least not for the cases investigated so far).

The code FLOCS (flow code for stellarators), that we developed and that is described in this paper, computes the radial particle fluxes and the bs current in stellarators. We consider a fully-ionized proton–electron plasma with parameters typical of a reactor. Both species are effectively treated simultaneously and are described as perturbed Maxwellians. The species are not ascribed to particular asymptotic collision-frequency regimes but are distributed according to the dependence of their Maxwellian on energy. The radial ambipolar electric field is determined self-consistently. The radial fluxes for that electric field determine the particle confinement time.

Whereas computation of particle fluxes in stellarators tends to concentrate on the region in velocity space where the parallel velocity of the particles is small, i.e., where particles are trapped in magnetic wells, the computation of the parallel current must deal with the entire velocity space. The trapped/untrapped transition region is of particular importance for the current, though, in that the boundary condition there is responsible for driving the current. Our code, FLOCS, handles both aspects appropriately and, as a result, it is able to compute the bs current in addition to the radial fluxes. Also, because FLOCS considers the complete velocity space ($0 \leqslant v_{\|} \leqslant v$ and in principle $0 \leqslant v < \infty$), it has the capability of incorporating momentum-restoring terms in the collision operator, which make sure that momentum is conserved during Coulomb collisions. These terms are known to affect the

bs current considerably in an axisymmetric tokamak; in stellarators, the situation is less clear.

In this paper we give a comprehensive account of the physics questions and the numerical issues incorporated in and addressed by the bounce-averaged transport code FLOCS. Our work is based on a logic similar to that employed in the 2 D Fokker–Planck code FPSTEL developed by Mynick and Hitchon [3] and Hitchon and Mynick [4], a code designed to compute the radial particle fluxes of a single species with a given energy. Our code can be considered as an improved and extended version of FPSTEL. Although familiarity with the treatment of Refs. [3, 4] might help to better understand the present paper, we provide the reader here with the necessary features of FPSTEL, so as to show how our work differs from and builds upon the work reported in the aforementioned papers.

This paper is organized as follows. In Section II, we review the basic neoclassical transport mechanisms in stellarators and comment briefly on the present status of stellarator-transport calculations. In addition, Section II gives us the opportunity to define our symbols. Section III deals with a description of the bounce-averaged Fokker–Planck code FPSTEL. Then, in Section IV, the physics embedded in our newly developed code FLOCS is explained in some detail. In Section V, we focus on the numerical implementation. Section VI represents some results obtained with FLOCS. Section VII summarizes the paper.

II. Basic Concepts of Neoclassical Stellarator Transport and Status of Computational Efforts

In this section we summarize the current status of stellarator neoclassical transport, the bulk of which consists of ripple transport. Our discussion is short because recent reviews have described analytic ripple transport computations (Kovrizhnykh [5]) and numerical studies (Beidler [6]).

The simplest model for $mod(\mathbf{B})$ along a field line, which has the features of standard stellarators, can be represented by

$$B = B_0(1 - \varepsilon_t \cos\theta - \varepsilon_h \cos(l\theta + m\zeta)); \tag{1}$$

$\varepsilon_t = r/R$ is the amplitude of the sinusoidal variation due to the toroidal field, whereas ε_h is the amplitude of the helical ripple (Fig. 1). An exact expression for ε_h can be quite complicated [7, 8], but for the present purposes we set $\varepsilon_h = \varepsilon_{h0} r^l$, where ε_{h0} is a constant and r is a typical minor radius, defined below. The integers l and m are the stellarator multipolarity and the number of field periods, respectively.

The configuration space has been parameterized by the flux coordinates (Ψ_t, θ, ζ), with θ the poloidal angle and ζ the toroidal angle, oriented as in Fig. 2.

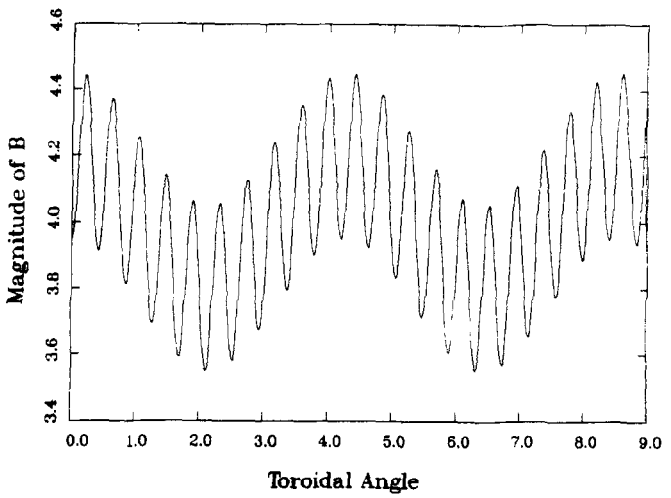

FIG. 1. Variation of mod B along a field line in a stellarator with $l = 2$, $m = 12$, $\iota = 1.47$, $\varepsilon_h/\varepsilon_t = 1.26$. B is expressed in Tesla (from Ref. [6]).

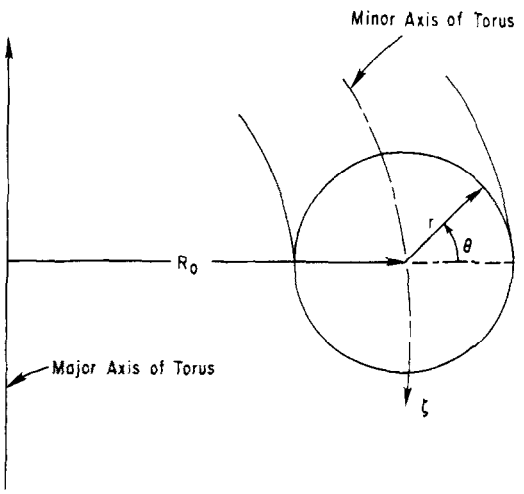

FIG. 2. Orientation of the (r, θ, ζ) coordinate system.

$2\pi\Psi_t$ is the toroidal magnetic flux enclosed by a flux surface. Rather than working with Ψ_t, however, it is convenient to work with an effective radius [3]

$$r(\Psi_t)=\left(\frac{2\Psi_t}{B_0}\right)^{1/2}. \tag{2}$$

Particles with low $v_{||}$ can become trapped by the helical ripples. While trapped they drift away from the field line due mainly to grad-B and $E\times B$ drifts. In combination with collisions, these deviations give rise to a random walk and hence diffusion.

A convenient way to characterize the trapping state of a particle in a ripple well is by means of the ripple-depth parameter y defined as

$$y\equiv\frac{B_{\text{turning}}-B_{\min}(\text{ripple well})}{B_{\max}(\text{ripple well})-B_{\min}(\text{ripple well})}. \tag{3}$$

Using the usual approximation that $\alpha\equiv\varepsilon_t\iota/(m\varepsilon_h)\ll 1$, this becomes

$$\begin{aligned} y&=\left[\frac{K}{\mu B_0}-(1-\varepsilon_t\cos\theta-\varepsilon_h)\right]\Big/(2\varepsilon_h)\\ &\equiv k^2\ (\text{most references}); \end{aligned} \tag{4}$$

K, μ, and ι are the kinetic energy, the magnetic moment $m_a v_\perp^2/2B$, and the rotational transform, respectively (m_a is the mass of species a). $B_{\text{turning}}=K/\mu$ is the value of B where the particle bounces, i.e., where $v_{||}=0$. $B_{\max}$ and $B_{\min}$ are the local maximum and minimum of the ripple well, respectively. We also indicated that the usual symbol employed is k^2. We use y rather than k^2 for agreement with Refs. [3, 4].

Particles with $0\leqslant y<1$ are ripple trapped, while those with $y>1$ are either toroidally blocked or passing. y is not a constant of the motion, in contrast to μ. y is related to the velocity-space variables K and μ. The variable y is very well suited to describe the trapping state of a particle.

A particle moving along a field line sees its y change when the field line travels from the outside of the device ($\theta=0$) to the inside ($\theta=\pi$), because B changes underneath it. Further, radial motion changes the electrostatic potential Φ and thus K, without changing the total energy $E=K+q\Phi$ or μ. As a consequence, particles that have a y near 1 can become trapped or detrapped by moving in θ or r.

Collisions can change the pitch angle, i.e., the ratio $v_{||}/v_\perp$, of a particle gradually (via small-angle deflections) and alter its μ and hence y. Thus, collisions can also influence the trapping state of particles. This is known as collisional entrapping and detrapping, to distinguish it from the collisionless process just described. A 90° deflection in velocity-space pitch angle, from $\mu=0$ or $y\to\infty$, to $\mu=K/B_{\min}$ or $y=0$ takes a time of roughly $\nu_\perp^{-1}$. To detrap a particle from the trapped region to a just-untrapped state requires less time; it happens at a rate $\nu_{\text{eff}}\equiv\nu_h=\nu_D/(2\varepsilon_h)$

since ripple-trapped particles occupy only a fraction $\sim(2\varepsilon_h)^{1/2}$ of the velocity space. ($v_D \equiv v_\perp/2$, where $v_\perp$ is that defined in the "NRL Plasma Formulary" [9].)

The analytic kinetic computations in the literature concentrate mainly on the ripple-trapped region and usually ignore the region $y > 1$ (but see Mynick [10] and Beidler *et al.* [11] for exceptions to this). For diffusion, a "bounce-averaged" (ba) formalism is usually adequate. All quantities involved related to ripple-trapped particles are time averaged between the bounce points in a helical-ripple well by means of a ba operator. The ba procedure usually assumes that the ripple wells are symmetric. In the limit of low rotational transform per field period, $\iota/m \to 0$, motion along the field line is equivalent to moving in ζ only, while θ remains constant. The larger the number of ripples per toroidal trough, when moving along a field line, the more accurate the ba procedure becomes. The peculiarities of the ba process have been examined and discussed by Beidler [6].

The drift-kinetic equation on which the analysis is based is the usual one: $(\mathbf{v}_\parallel + \mathbf{v}_\perp)\cdot\nabla f = C(f)$. A linearization about a Maxwellian f_M is performed. Bounce averaging over a helical ripple (denoted by angle brackets $\langle\ \rangle$) removes the $\mathbf{v}_\parallel\cdot\nabla$ term in the ripple-trapped region. The ba equation for $\langle f_1\rangle = \langle f\rangle - f_M$ is (neglecting small beating terms) [3, 4]

$$\langle\dot r\rangle\frac{\partial f_M}{\partial r} + \langle\dot\theta\rangle\frac{\partial\langle f_1\rangle}{\partial\theta} + \langle\dot y\rangle\frac{\partial\langle f_1\rangle}{\partial y} = \langle C_y(\langle f_1\rangle)\rangle, \tag{5}$$

in (E, y) variables. Here $\langle\dot r\rangle$, $\langle\dot\theta\rangle$, and $\langle\dot y\rangle$ are the phase-space velocities: $\dot r$ stands for $\mathbf{v}_D\cdot\nabla\Psi/|\nabla\Psi|$, with $\mathbf{v}_D$ the perpendicular guiding-center drift, while $\langle\dot y\rangle \equiv \dot y$ equals $\partial y/\partial\theta\langle\dot\theta\rangle + \partial y/\partial r\langle\dot r\rangle$, describing the changes in y, including collisionless entrapping and detrapping. This variation in y, produced by flow, is only important at very low collision frequencies since collisions cause the dominant changes in y, otherwise. The term $\langle\dot r\rangle\,\partial f_M/\partial r$ acts as the driving term in the equation. $\langle C_y\rangle$ is the collision operator expressed in terms of y. Since the variable y characterizes the degree to which a particle is helically trapped, it is the natural variable to be used in a ba formalism.

According to the relative magnitudes of the frequencies $\langle\dot\theta\rangle$ and ν_h, the latter appearing in $\langle C_y\rangle$, one distinguishes three asymptotic collision-frequency regimes. They are characterized by the dependence of the diffusion coefficient on the collision frequency. One has the ν, $\nu^{1/2}$, and ν^{-1} regimes from low to high collision frequency. (See Refs. [5, 6] for the physical mechanisms and relevant references.)

Recently, a "unified theory of ripple transport in stellarators" has been developed by Beidler *et al.* [11, 6]. The three usual asymptotic regimes are all considered simultaneously. The authors employ an extension of the solution scheme commonly used for the $\nu^{1/2}$ regime. The results of this unified theory were compared with several numerical results (Monte Carlo, FPSTEL, and DKES, all to be discussed below), and the agreement is remarkable.

As we alluded to above, particles that become detrapped will most likely be toroidally blocked. These particles undergo radial diffusion essentially similar to

banana diffusion in an axisymmetric tokamak. Although these blocked particles do not exhibit pure banana-type diffusion because of non-axisymmetry and because of the influence of the ripple-trapped region on the blocked region, the simple addition of axisymmetric tokamak diffusion coefficients (banana-plateau) to the ripple trapping induced diffusion coefficients (ν, $\nu^{1/2}$, ν^{-1}) gives an adequate estimate for the expected overall transport. An example of the numerical results obtained from FPSTEL [4] for a single ion species versus the asymptotic analytic results for tokamaks and stellarators is shown in Fig. 3.

The total radial particle flux in non-axisymmetric devices is not automatically ambipolar, in the sense in which this is true in an axisymmetric device [13] because conservation of toroidal angular momentum in not guaranteed in these machines. Since one of the species will be lost faster than the other, a (mainly) radial electric field will be set up. The steady-state electrostatic field is obtained from the constraint

$$\sum_a q_a \Gamma_a = 0, \tag{6}$$

in which q_a and Γ_a represent the electric charge and the flux-surface averaged radial flux, respectively. (In Ref. [12] we have considered the ambipolarity issue in detail.)

Besides purely kinetic computations, attempts to compute radial fluxes and parallel flows and currents have been undertaken via a moment-equation approach, which originates with Hirshman [1, 14].

Shaing and Callen [2] generalized the Hirshman formalism to non-axisymmetric magnetic fields and set the framework for stellarator geometries. This and sub-

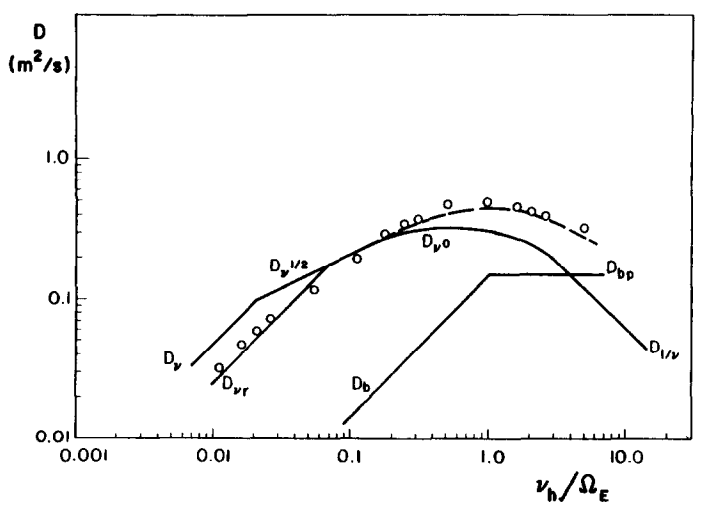

FIG. 3. Comparison of numerical results obtained from FPSTEL [4] with analytic results. D_b and D_{bp} are the tokamak banana and plateau regimes, respectively. The upper solid line represents the stellarator ripple-diffusion coefficient. The dashed line is the sum of ripple and banana transport.

sequent treatments [15–22], however, have been limited to the higher-frequency regimes ($1/\nu$, plateau, and Pfirsch–Schlüter); typical stellarator regimes, $\nu^{1/2}$ and ν have not been considered.

In the moment-equation approach, the radial fluxes and the parallel currents are expressed in terms of the flux-surface averaged toroidal and parallel components of the viscous-force density. The latter are computed from kinetic theory, showing that they are proportional to (generalized) poloidal and toroidal flows. The advantage of the moment-equation approach is that momentum conservation of the collision operator is easily incorporated in the formalism.

The bootstrap current originates from the trapped-passing particle dynamics and is thus related to the same processes which are responsible for neoclassical radial diffusion. According to the kinetic picture, this current is driven by the momentum present in the trapped population immersed in a pressure gradient (a *diamagnetic-like* flow carried by particles with closed orbits). In the fluid-based model, the bootstrap current is explained as the difference between parallel ion and electron flows resulting from the *viscous damping* of the electron flow, by the trapped population.

The theory behind the bootstrap current in axisymmetric tokamaks is quite well understood. In stellarators, the situation is less clear, because of the different classes of trapped particles. Presently, it is widely accepted [5, 2, 20] that a non-zero bs current is predicted by kinetic neoclassical theory in the lower collision-frequency regimes. Specifically, the bs current is driven by the parallel viscous-force density $\langle\langle \mathbf{B}\cdot\nabla\cdot\boldsymbol{\Pi}_e \rangle\rangle$ [21], which is given by $\langle\langle B\int d^3v m_e v_{\|}(v_{\|}\hat{B}\cdot\nabla f^e)\rangle\rangle$. (The double angle brackets represent the flux-surface average.)

The most obvious way to compute the current in stellarators is via its definition, $\mathbf{J} = ne(\mathbf{u}_i - \mathbf{u}_e)$. The fluid flows $\mathbf{u}_j$ are the $\mathbf{v}$ moments of f^j. FLOCS computes the bs current as $J_{\|} = ne(u_{\|i} - u_{\|e})$, in which the parallel flows are computed numerically as the $v_{\|}$ moments of f^j.

Previous numerical computations of stellarator neoclassical transport have been developed along three lines: Monte Carlo simulations, a variational solution of the drift-kinetic equation (DKES), and a finite-differencing approach to solving the ba drift-kinetic equation (FPSTEL). For Monte Carlo techniques, we refer to Beidler [6]. Some physics issues, relevant to our code FLOCS, addressed by DKES, are touched upon momentarily. A short description of the ideas incorporated in FPSTEL is given in the next section.

Hirshman *et al.* [23] have developed a numerical code to solve the linearized drift-kinetic equation, in which collisions are modeled by the Lorentz operator. The solution involves a variational principle in which the trial functions are expanded in a Fourier–Legendre series. Further, the approach relies on a very efficient numerical matrix-inversion scheme.

To make the method work, a self-adjoint form of the kinetic equation is required. As a consequence, some compromises as to the physics had to be made. Rather than projecting onto a drift surface, the particle motion is projected onto a flux surface. This implies that the radial excursion off a flux surface is disregarded in the change

of the pitch angle. The approximation is valid for particles far away from the trapping/detrapping boundary in phase space, but it distorts the collisionless trapping/detrapping process substantially. When a particle moves radially outward in the presence of a large radial electric field it sees its kinetic energy changed, $\Delta K = E - q\,\Delta\Phi$. Since the particle has a constant μ, a small radial excursion thus can provide enough parallel kinetic energy to make it detrap: an amount $\Delta K_{\|} = \varepsilon_h K$ will certainly detrap the particle. Hence the trapping/detrapping physics is not correctly described by DKES. This is one of the reasons why the radial particle fluxes computed by DKES are insensitive to the sign of the electric field. See also Ref. [24].

The DKES code can handle complicated magnetic geometries; the number of harmonics in B kept is virtually unlimited. No bounce averaging over a helical ripple is performed.

Although the physics embedded in DKES does not allow a proper description of the particle orbits, implying an implicit insensitivity to the sign of the radial electric field, it should be pointed out that this does not seem to matter too much for computation of the transport coefficients, as can be concluded from comparison with other numerical results (in the parameter regimes investigated so far) [3, 6]. The codes FPSTEL [3, 4] and FLOCS, to be described in this paper, do describe the "sickle-shaped" and "deformed-circle" particle trajectories, for the two signs of the electric field, quite accurately. However, they do not seem to show a "significant" dependence of the diffusion coefficient on the sign of E_r, because in the $\langle \dot{\theta} \rangle$ phase-space flow velocity the $\langle \cos \eta \rangle$ term is neglected and (effectively) only the Ω_E term is kept (apart from a small correction to make the divergence condition satisfied —see Eq. (20), below). (A possible boundary-layer effect due to a discontinuous jump of the particle trajectories which depends on the sign of the electric field, has not yet manifested itself for the configurations and computations considered.) The original discrepancy between the results of Ref. [4] and what DKES predicted [11] for the so-called transport-optimized stellarators (σ cases) has been resolved by Beidler [6], by renormalizing the abscissa of Fig. 3 to $\nu_h / \langle \dot{\theta} \rangle$.

III. Bounce-Averaged Fokker–Planck Code for Stellarators (FPSTEL)

We now give a fairly complete description of the ba Fokker–Planck code developed by Mynick and Hitchon [3, 4]. This work establishes the framework upon which our computation, to be discussed in the next section, will be based. We shall emphasize those issues which are important for our problem.

The code FPSTEL computes the distribution function as a function of two variables, y and θ, for a single species. The radial position of the particles is roughly constant because the radial drift velocity is small. Therefore f is computed at a constant radius, reducing r to a parameter. Attention should be drawn to the fact that although $\dot{r}$ is small, it is properly incorporated in the driving term. Also,

its influence on the change of y, i.e., $\dot{y}$, is taken into account in order to describe collisionless trapping and detrapping accurately. As explained in Ref. [3], the "small" term $\langle \dot{r} \rangle \partial \langle f_1 \rangle / \partial r|_y$ is neglected but not the term $\langle \dot{r} \rangle \partial \langle f_1 \rangle / \partial r|_\mu$; conversion from μ to y as a variable, generates an important term in the expression for $\dot{y}$.

Collisions are modeled with a Lorentz operator in which the collision-frequency parameter ν can be changed through its energy and density dependence. Energy scattering is absent, allowing the computation to be done on a constant-energy shell, the kinetic energy being equal to the thermal energy.

Since the computations are done on a flux surface, $r =$ constant, kinetic energy and total energy are equivalent. Caution is needed, however, when derivatives with respect to r are taken.

The kinetic equation, "*time averaged over a helical ripple*," can be expressed in a form similar to Eq. (5). However, one should distinguish between $y < 1$ and $y > 1$. The averaging operator will annihilate the $\mathbf{v}_{\|} \cdot \nabla f = v_{\|} \partial f / \partial l$ term in the equation for ripple-trapped particles (which have $y < 1$); for those particles $\partial \langle f \rangle / \partial l \equiv 0$, since $\langle f \rangle$ is a true *bounce average*. For non-ripple-trapped particles ($y > 1$), the equation is merely *time averaged over the time it takes a particle to cross a ripple well* [3], and although $\langle f \rangle|_{y>1}$ is independent of the small-scale variations of l, due to the ripples, it is not constant on the large scale length of several ripples. For particles with $y > 1$, the $v_{\|} \partial f / \partial l$ term becomes after time averaging $\langle v_{\|} \rangle \partial \langle f \rangle / \partial l_{av} = [\langle v_{\|} \rangle / (R/\iota)] \partial \langle f \rangle / \partial \theta$, since $dl_{av} = (R/\iota)\, d\theta$. So, $\langle f \rangle|_{y>1}$ is not a bounce-averaged distribution function in the literal sense, only averaged over the time it takes to cross a helical ripple; we attached a subscript "*av*" to l to stress that $\langle f \rangle|_{y>1}$ is only sensitive to slower variations in l.

Compactly written, the equations read:

$$y < 1: \quad \frac{\partial \langle f_1 \rangle}{\partial t} + \langle \dot{\theta} \rangle_< \frac{\partial \langle f_1 \rangle}{\partial \theta} + \dot{y}_< \frac{\partial \langle f_1 \rangle}{\partial y} - \langle C(\langle f_1 \rangle) \rangle = - \langle \dot{r} \rangle \frac{\partial f_M}{\partial r} \tag{7}$$

$$y > 1: \quad \frac{\partial \langle f_1 \rangle}{\partial t} + \langle \dot{\theta} \rangle_> \frac{\partial \langle f_1 \rangle}{\partial \theta} + \dot{y}_> \frac{\partial \langle f_1 \rangle}{\partial y} - \langle C(\langle f_1 \rangle) \rangle = - \langle \dot{r} \rangle \frac{\partial f_M}{\partial r}. \tag{8}$$

We have attached subscripts $<$ and $>$ to the phase-space velocities $\langle \dot{\theta} \rangle$ and $\dot{y}$, according to whether they must be used for $y < 1$ or $y > 1$. The radial drift velocity $\langle \dot{r} \rangle$ is the average of $\dot{r}$, given underneath Eq. (5), while the poloidal precession frequencies are given by

$$\langle \dot{\theta} \rangle_< = \langle \dot{\theta}_{ph} \rangle, \tag{9}$$

$$\langle \dot{\theta} \rangle_> \simeq \frac{\iota}{R} \langle v_{\|} \rangle. \tag{10}$$

For $y < 1$, only the perpendicular guiding-center drift, $\langle \mathbf{v}_D \cdot \nabla \theta \rangle \equiv \langle \dot{\theta}_{ph} \rangle$, survives since $\langle v_{\|} \rangle (y < 1) \equiv 0$. For toroidally-blocked and passing particles, the average free-streaming part dominates over the $\dot{\theta}_{ph}$ term by several orders of magnitude so

that the latter can be neglected. The phase-space velocities $\dot{y}$ are related to $\dot{r}$ and the respective $\dot{\theta}$'s via the expression given underneath Eq. (5).

Equations (7) and (8) are not averaged equations in the exact sense. Rather, they are equations in which all quantities have been averaged; the product of the averages instead of the average of the product has been taken. Consequently, the equations are approximations to the true averaged equations, in which small beating terms have been neglected.

FPSTEL computes the particle fluxes due to ripple-trapped and toroidally-blocked particles in the low-collision-frequency regimes. Therefore, an explicit *assumption* throughout the code has been made that $y \ll \varepsilon_h^{-1}$, implying from Eq. (3) that $K \simeq \mu B_0 \simeq \mu B$. In the next section, we shall give more general expressions holding for large y values and point out how to recover the simplified forms which hold for $K \simeq \mu B_0$.

The magnetic-field geometry in the Mynick and Hitchon [3] paper has been chosen such that $\hat{B} \sim -\hat{\zeta}$; the toroidal field points in the negative $\hat{\zeta}$ direction.

Helically-trapped particles are described next. For particles with small y values, for which FPSTEL is applicable, $v_{\|}^2 \ll v_{\perp}^2$ and the grad B drift is dominant over the curvature drift. The ripple-averaged guiding-center-drift velocity is approximately

$$\langle v_B \rangle = \frac{\mu B}{m_a \omega_c R} = \frac{K}{m_a \omega_c R}. \tag{11}$$

($\mathbf{v}_B$ is the grad B part of $\mathbf{v}_{D\perp}$; m_a represents the mass of species a.) The radial and poloidal components of the (roughly vertical) drift are

$$\langle \dot{r} \rangle = \langle v_B \rangle \sin\theta, \qquad \langle \dot{\theta}_B \rangle = \frac{\langle v_B \rangle}{r} \cos\theta. \tag{12}$$

(A more correct expression for $\langle \dot{\theta}_B \rangle$ would contain a term proportional to $\langle \cos\eta \rangle$, where η is the ripple phase, $\eta = l\theta + m\zeta$ [6]. Since this part of the poloidal precession, as well as that given by Eq. (12b), is assumed to be completely overshadowed by the poloidal $E \times B$ drift, to be discussed next, it need not be considered.)

The $E \times B$ drift velocity due to a radial ambipolar electric field is within the flux surface and is roughly in the poloidal direction:

$$\langle \dot{\theta}_E \rangle \equiv \langle \Omega_E \rangle = \frac{qE_r}{m_a \omega_c r} = \frac{E_r}{rB}. \tag{13}$$

As for any $E \times B$ drift, Ω_E is independent of the species.

The total ba poloidal velocity for $y < 1$ does not contain any free-streaming so that we have

$$\langle \dot{\theta} \rangle_< = \langle \dot{\theta}_{ph} \rangle = \langle \dot{\theta}_B \rangle + \langle \Omega_E \rangle. \tag{14}$$

Typically, one has that $\dot{\theta}_B/\Omega_E \sim \varepsilon_t/(q\Phi/T)$ which is small for the expected potentials, which are of the order of the temperature. The subscript *ph* indicates that $\dot{\theta}_{ph}$ is the *physical* poloidal drift frequency in contrast to the numerical one, $\dot{\theta}_n$, which will be introduced momentarily.

To find an expression for the phase-space velocity $\dot{y}$, one could use its definition in terms of the r and θ phase-space flows, $\langle \dot{y} \rangle \equiv \dot{y} = \partial y/\partial\theta \langle \dot{\theta} \rangle + \partial y/\partial r \langle \dot{r} \rangle$. However, straightforward computation with the approximate drift velocities of Eqs. (12) and (14) does not provide an accurate enough result because the leading-order terms of $\partial y/\partial\theta\langle\dot{\theta}\rangle$ and $\partial y/\partial r\langle\dot{r}\rangle$ cancel each other. What is left is of the same order as the error made in the approximations used to obtain the approximate drifts. Pursuing this exercise is useful though, because it demonstrates that the $\partial y/\partial r\langle\dot{r}\rangle$ term is important, in turn showing that the $\langle\dot{r}\rangle\,\partial\langle f_1\rangle/\partial r$ term can only be neglected in the kinetic equation after the conversion from μ to y has been performed.

As Mynick and Hitchon [3] recognized, a convenient and accurate way to find $\dot{y}_<$ is from the invariance of the second adiabatic invariant $I \equiv \oint dl\, m_a v_{||}$. I has been computed in Ref. [3], and, for an $l=2$ stellarator (for which $\varepsilon_h = \varepsilon_{h0} r^2$), it was found to be proportional to $rA(y)$, where $A(y)$ is a combination of elliptic integrals. Conservation of I implies that $d/dt(rA(y))=0$, or that

$$\dot{y}_< = -\frac{\langle \dot{r} \rangle}{r}\frac{A}{A'}. \tag{15}$$

The dot represents a total time derivative and the prime indicates differentiation with respect to the argument, here y. Expressions for A and A' are given in Ref. [3].

FPSTEL solves the kinetic equation via relaxation of its finite-difference equivalent. To guarantee numerical conservation of particles, the equation is converted to *conservation form*. To do this, the divergence of the phase-space flow must be zero:

$$\frac{1}{\langle J \rangle}\left[\frac{\partial\langle J\rangle\langle\dot{r}\rangle}{\partial r} + \frac{\partial\langle J\rangle\langle\dot{\theta}\rangle}{\partial\theta} + \frac{\partial\langle J\rangle\langle\dot{y}\rangle}{\partial y}\right] = 0. \tag{16}$$

Here $\langle J \rangle$ is the (averaged) Jacobian, expressed in the variables (r, θ, E, y).

To check whether Eq. (16) is satisfied, the Jacobian must be specified. From Ref. [3],

$$\langle J \rangle_< \simeq 4\pi r R \frac{B_0^{1/2}}{m_a^{3/2}} (\varepsilon_h \mu)^{1/2} A' \simeq 4\pi r R \frac{(\varepsilon_h K)^{1/2}}{m_a^{3/2}} A'. \tag{17}$$

With this Jacobian, $\langle J \rangle \propto r^2 A'(y)$, Mynick and Hitchon [3] write

$$\frac{\partial\langle J\rangle\langle\dot{r}\rangle}{\partial r} = -2\frac{\partial\langle J\rangle\langle\dot{y}\rangle}{\partial y} = -2\frac{\partial\langle J\rangle\langle\dot{\theta}_B\rangle}{\partial\theta} \tag{18}$$

and therefore that

$$\frac{\partial\langle J\rangle\langle\dot{r}\rangle}{\partial r}+\frac{\partial\langle J\rangle\langle\dot{y}\rangle}{\partial y}+\frac{\partial\langle J\rangle\langle\dot{\theta}_{ph}\rangle}{\partial\theta}=0, \tag{19}$$

since $\langle\Omega_E\rangle$ and $\langle J\rangle$ are independent of θ. In Ref. [3] a typographical error has occurred in the sign of the y derivative in Eq. (18).

We should like to draw attention to a minor inaccuracy in the derivation of Eq. (19) in Ref. [3]. The divergence, Eq. (19), is to hold for the set of variables (r, θ, y), i.e., with r still considered as a variable. However, the r derivative in Eq. (19) is to be taken at constant total energy E. The Jacobian $\langle J\rangle$ of Eq. (17) is expressed in terms of the kinetic energy $K=E-q\Phi(r)$, and so the $\partial/\partial r$ would give rise to an electric field term $\Phi'(r)$. This neglect has no repercussions, however, because a correct computation, in which the θ dependence of $\langle J\rangle$ is kept by not replacing μ by K/B_0, shows that this electric field term contribution is canceled by the $\langle\Omega_E\rangle\,\partial\langle J\rangle/\partial\theta$ term. (The θ-dependent $\langle J\rangle$ is considered in the next section.) For the given drift velocities (which are themselves accurate to order ε), the divergence condition is satisfied exactly.

A second reason why this omission in $\partial/\partial r$ is not very important is because in the code FPSTEL r is eliminated as a variable. The form of $\langle J\rangle$ as expressed in Eq. (17) is postulated as the correct one. To make the divergence condition be satisfied in two variables (θ, y), it is obvious from Eq. (18) that either $\dot{y}$ or the θ-dependent part of $\langle\dot{\theta}\rangle_<$ should have the other sign. Therefore, Mynick and Hitchon [3] construct an appropriate $\langle\dot{\theta}\rangle_<$ for the numerical code

$$\langle\dot{\theta}\rangle_< \equiv \langle\dot{\theta}_n\rangle_< \equiv \langle\Omega_E\rangle-\langle\dot{\theta}_B\rangle, \tag{20}$$

to *replace* the physcially correct $\langle\dot{\theta}_{ph}\rangle$ of Eqs. (14) and (12). This approximation gives rise to an error of order ε_t, which is acceptable for the usual large-aspect-ratio stellarators. We have then for the two-dimensional divergence:

$$\frac{\partial\langle J\rangle\langle\dot{y}\rangle}{\partial y}+\frac{\partial\langle J\rangle\langle\dot{\theta}_n\rangle_<}{\partial\theta}=0. \tag{21}$$

For untrapped particles matters are simpler. The $\langle\dot{\theta}\rangle_>$ velocity is related to the free-streaming parallel velocity as indicated in Eq. (10). The parallel velocity, time averaged over a ripple well, is [3]

$$|\langle v_{\|}\rangle| = \frac{\int_h dl}{\int_h dl/|v_{\|}|}=\frac{\hat{u}}{A'}. \tag{22}$$

Here $\hat{u}$ equals

$$\hat{u}=2\left(\frac{\varepsilon_h\mu B_0}{m_a}\right)^{1/2}. \tag{23}$$

Hence,

$$\langle \dot{\theta} \rangle_> = \sigma \frac{\iota}{R} \frac{\hat{u}}{A'}, \tag{24}$$

σ being the sign of $v_{||}$.

To find $\dot{y}_>$, we observe that the radial drift velocity $\dot{r}$ can be neglected for $y > 1$ in comparison with the rapid parallel motion. For $y > 1$ we can find $\dot{y}$ from its definition,

$$\dot{y}_> = \langle \dot{\theta} \rangle_> \left. \frac{\partial y}{\partial \theta} \right|_\mu = -\frac{\varepsilon_t}{2\varepsilon_h} \langle \dot{\theta} \rangle_> \sin\theta. \tag{25}$$

For these phase-space flows it is readily checked that the two-dimensional divergence condition is satisfied since

$$\frac{\partial}{\partial \theta} (\langle J \rangle \langle \dot{\theta} \rangle_>) = 0 = \frac{\partial}{\partial y} (\langle J \rangle \dot{y}). \tag{26}$$

The Jacobian $\langle J \rangle$ for $y > 1$ is given by half the Jacobian for trapped particles because the summation over σ is absent now: $\langle J \rangle_> = \frac{1}{2} \langle J \rangle_<$.

The reason for including the region $y > 1$ in FPSTEL is because the distribution function for $y > 1$ must match the distribution function for $y < 1$ at the $y = 1$ boundary. This is a significant improvement over the assumption that $f = f_M$ for $y > 1$, typically made in the older literature.

The driving term $\langle \dot{r} \rangle \partial f_M / \partial r$ is written in terms of a scale length, L_a, defined by

$$\langle \dot{r} \rangle \frac{\partial f_M}{\partial r} \equiv -\frac{\langle \dot{r} \rangle f_M}{L_a}. \tag{27}$$

The choice of L_a represents the radial profile; in Refs. [3, 4] $L_a = a$, where a is the minor radius.

Thc ba form of the Lorentz collision operator, $C_L(f)$, in E (or K) and μ variables is [3]

$$\langle C_L(\langle f \rangle) \rangle = \frac{\nu_D}{B} \frac{\partial}{\partial \mu} \left(I\mu \frac{\partial \langle f \rangle}{\partial \mu} \right) \Big/ \frac{\partial I}{\partial E}, \tag{28}$$

in which I is the bounce-action integral mentioned above. (For non-ripple-trapped particles I is a time average over a helical well, as usual; as for the Jacobian $I_> = I_</2$. The total I_{tot} for toroidally blocked particles is the sum of the I values over each ripple well. I itself is not a constant of the motion for non-ripple-trapped particles.) Using the well-known fact that [3]

$$\tau_b = \left. \frac{\partial I}{\partial E} \right|_\mu = \frac{2}{\hat{u}} A'(y) L_h, \tag{29}$$

$\langle C_L(\langle f\rangle)\rangle$ in terms of E (or K) and y variables is

$$\langle C_L(\langle f\rangle)\rangle \simeq \frac{\nu_h}{A'}\frac{\partial}{\partial y} A \frac{\partial\langle f\rangle}{\partial y}. \tag{30}$$

Here $\nu_h = \nu_D/2\varepsilon_h$, $\nu_D = \nu_\perp/2$, and L_h is the length of a helical ripple measured along a field line. This expression will be retrieved as a simplified form, appropriate for low y values, from the more general expression which we shall derive in the next section.

The phase-space flows $\dot{y}$ and $\langle\dot{\theta}\rangle$ computed above can be represented in the $\theta - y$ plane [3]. Three kinds of orbits can be distinguished.

The first class of particles are *passing* particles. They never hit the $y = 1$ boundary and consequently cannot become entrapped collisionlessly. These particles circulate in the positive or negative θ direction, according to their direction of flow along the field line.

The second category of particles is *ripple trapped* with a low enough y value to avoid collisionless detrapping. These particles' helical bananas precess poloidally due to the $E \times B$ drift. For a positive (negative) electric field, they move in the positive (negative) θ direction. In contrast to the group of passing particles, whose θ motion is bidirectional (in accordance with their thermal motion), ripple-trapped particles, in the ba formulation, flow unidirectionally in θ.

The set of particles with intermediate y values are called *transiting* particles. Part of the time, they are known as toroidally blocked particles (as long as they have $y > 1$). When they reach the $y = 1$ boundary, they usually reflect, but have a small chance ($\sim 1\,\%$) to become entrapped in a helical ripple well.

Bounce averaging over a helical ripple eliminates all information concerning the ripple phase η. As a result, detailed knowledge of the position where a particle can entrap collisionlessly is not available. To circumvent this complication, Mynick and Hitchon [3] make use of Liouville's theorem to compute the fraction of particles that entraps when reaching the $y = 1$ boundary. Liouville's theorem states that the distribution function is constant along a phase-space trajectory in the absence of collisions. Therefore, the trapping probability can be determined by matching the y fluxes on neighboring mesh points on either side of the $y = 1$ boundary when $\langle f_f\rangle = \langle f_t\rangle$:

$$p_{ft} = \frac{\langle J\rangle\, \dot{y}(\theta, 1 - \Delta y/2)}{\langle J\rangle\, \dot{y}(\theta, 1 + \Delta y/2)}. \tag{31}$$

The subscripts f and t stand for *forward* and *trapped*, respectively. Forward particles are those that have a finite probability of becoming entrapped when hitting the $y = 1$ boundary. (*Backward* particles are those that must reflect at $y = 1$. After reflecting, they again become forward particles.) $\langle f_f\rangle$ and $\langle f_t\rangle$ are the distribution functions for forward and trapped particles, respectively; they have been canceled in Eq. (31) because in the collisionless case (and in the absence of the driving term)

they are equal to each other, evaluated at $y = 1^-$ and $y = 1^+$, respectively. Δy is the mesh spacing.

A detailed explanation of the connection between Liouville's theorem and the trapping probability has been given in Ref. [3]. The trapping probability was generalized for cases where ε_h is θ dependent in Ref. [4].

It has been pointed out [3] that the splitting of $\langle f_f \rangle$ into $\langle f_b \rangle$ and $\langle f_t \rangle$ at the entrapping side in θ, and the recombination of $\langle f_b \rangle$ and $\langle f_t \rangle$ into $\langle f_f \rangle$ for opposite values of θ, in combination with the approximate expressions used for the phase-space velocities leads to a physical inconsistency.

To avoid it, the authors of Ref. [3] have assumed that the backwards steady-state solution is artificially reduced by a fraction equal to the trapping probability:

$$f_{0t} = f_{0f} \equiv f_0(E, r), \qquad f_{0b} \equiv (1 - p_{ft})\, f_0(E, r). \tag{32}$$

The artificial suppression of $\langle f_b \rangle$ by a few percent gives rise to an aesthetically regrettable deformation of the contour plots for $\langle f \rangle$, but it does not influence the value for the radial flux. This is avoided in the present work.

To end this section on the code FPSTEL [3, 4], we say a few words about the numerical method used. A two-dimensional (θ, y) mesh is constructed to cover the range $\theta = 0$ to $\theta = 2\pi$ and $y = 0$ to $y = y_{\max}$, where $y_{\max} \sim 3$. The mesh spacings typically used range from $\Delta y \sim 0.05$ to 0.1 and $\Delta\theta \sim 2\pi/20$ to $2\pi/10$, the coarser mesh being sufficient for the higher collision-frequency regimes. The kinetic equation for $\langle f \rangle$ is solved by relaxation in a finite differencing scheme; the code is run until $\partial \langle f_1 \rangle / \partial t$ is negligible. The finite differencing itself is a hybrid between an explicit scheme and an implicit one, using intermediate iterations within the same time step. The stability of the explicit scheme is improved, as the propagation of information is akin to that in an implicit scheme.

The setup of the numerical scheme in this way allows the description of the time evolution of $\langle f_1 \rangle$, e.g., due to heating of the plasma or after pellet injection. If only the time-independent solution is of interest, an implicit scheme is likely to be more economical from a computational standpoint. No matter how the time integration is performed, it remains crucial, however, to have the *divergence condition*, Eq. (16), satisfied, because only then is the kinetic equation convertible into conservation form.

IV. Physics Issues Incorporated in FLOCS

a. *Introduction*

The distinction between this work and that of Mynick and Hitchon [3, 4] resides mainly in the fact that we wish to obtain a distribution function which allows meaningful computation of the parallel plasma currents. This requires that we consider both ions and electrons simultaneously for all velocity-space pitch angles

and over the full energy range. In addition, the distribution function must contain *sufficient* information about variations along a field line, as suggested by the relationship $\langle\langle J_{||} B\rangle\rangle \propto \langle\langle \mathbf{B}\cdot\nabla\cdot\mathbf{\Pi}\rangle\rangle = \langle\langle \ldots \partial f/\partial l\rangle\rangle$. We also have the possibility to check the importance of momentum-restoring terms in the collision operator.

A formalism based on "bounce averaging" over the helical-ripple wells in B is adequate for our purposes. The $\langle f_1\rangle$ we compute ignores certain details of the helical ripples, but contains the "tokamak-like" variation along the field line. Our $\langle f_1\rangle$ does include crucial stellarator-ripple features, in that the collisionless and collisional trapping and detrapping into and out of the helical-ripple wells are properly described. Hence, the drag exerted by trapped particles on toroidally-blocked particles (i.e., particles blocked in the tokamak-like trough) and indirectly on passing particles is incorporated.

A ba scheme is generally considered adequate for the computation of the radial fluxes. The exact position of a particle is not important for this purpose, but only its average position or, said differently, the position of the center of the small helical banana. These qualitative statements can be substantiated more rigorously from the definition for the radial flux, $\Gamma \propto \int \dot{r} f_1$, since we shall shortly show that the averaged radial-drift velocity, $\langle \dot{r}\rangle$, and its non-averaged remainder, $\dot{r} - \langle \dot{r}\rangle$, are of the same order of magnitude, while $\tilde{f}_1 \ll \langle f_1\rangle$. The validity of this last relationship has been shown in Ref. [25].

Careful consideration of this issue is necessary if the parallel currents are of concern. As we mentioned above, the bs current can be related to the parallel viscous-force density $\langle\langle \mathbf{B}\cdot\nabla\cdot\mathbf{\Pi}\rangle\rangle$. The latter is by definition given by the (flux-surface averaged) $mv_{||}$ moment of $v_{||}\,\partial f/\partial l$. Therefore, it is insufficient that $\tilde{f}_1 \ll \langle f_1\rangle$; rather the same relationship must hold for their respective variations along a field line.

From $\langle\langle J_{||}\rangle\rangle \propto \langle\langle \mathbf{B}\cdot\nabla\cdot\mathbf{\Pi}\rangle\rangle = \langle\langle \ldots \partial f/\partial l\rangle\rangle$, it is clear that the ripple-trapped particles ($y<1$), for which $\partial\langle f\rangle/\partial l \equiv 0$, do not contribute to the bootstrap current, in the ba formalism. For toroidally blocked and passing particles (which have $y>1$), however, $\partial\langle f\rangle/\partial l$ is finite (as is explained above Eq. (7)) and consequently, they carry the bootstrap current. $\langle f\rangle|_{y>1}$ contains the typical stellarator effects in that $\langle f\rangle|_{y>1}$ is connected smoothly onto $\langle f\rangle|_{y<1}$ at the $y=1$ boundary. (It should be emphasized that ripple-trapped particles, characterized by $\langle f\rangle|_{y<1}$, do not *carry* the bs current, but their distribution function does *drive* the stellarator part of it.) These features guarantee that, in addition to producing the tokamak-like bs current, $\partial\langle f\rangle/\partial l_{av}$ also incorporates the "overall" stellarator behavior. To quantify the word "overall" of the previous sentence, we have to establish that $\partial\langle f\rangle/\partial l_{\mathrm{av}} \gg \partial\tilde{f}/\partial l$, $\tilde{f}$ being defined by $\tilde{f} \equiv f - \langle f\rangle$ and $dl_{\mathrm{av}} = (R/\iota)\,d\theta$.

For typical stellarator-reactor parameters (as in Table I), the quantity $\partial\tilde{f}_1/\partial l$ is about an order of magnitude smaller than $\partial\langle f_1\rangle/\partial l_{\mathrm{av}}$. More specifically, in Ref. [25], we have estimated that $\partial\tilde{f}_1/\partial l \sim \tilde{f}_1/L_h$, and $\partial\langle f_1\rangle/\partial l_{\mathrm{av}} \sim \langle f_1\rangle/L_t$, with $L_h = 2\pi R/m$ and $L_t = R/\iota$. Since ions are roughly in the $\nu^{1/2}$ regime, while electrons find themselves in the $1/\nu$ regime, it is easy to show [25] that $\tilde{f}_1/\langle f_1\rangle < 0.01$ for both species. Therefore, $(\partial\tilde{f}_1/\partial l)/(\partial\langle f_1\rangle/\partial l_{\mathrm{av}}) \sim (\tilde{f}_1/\langle f_1\rangle)(m/\iota) \sim 0.1$. Consequently, the bs current and the parallel viscosity are well approximated by a ba scheme.

TABLE I

Major radius	20 m
Minor radius	2 m
Mean radius of magnetic surface studied	1 m
ε_t at 1 m	0.05
Magnetic field on axis	4 T
Multipolarity l	2
Field periods m	12
ε_h at 1 m	0.063
ι at 1 m	1.47
n at 1 m	$2.0 \times 10^{20}\ m^{-3}$
T at 1 m	12 keV
$\alpha_n \equiv -an'/n$	2.25
$\alpha_T \equiv -aT'/T$	0.01

The code FLOCS solves the same formal ba drift-kinetic equations for $\langle f_1 \rangle$ as those given in Eqs. (7) and (8). However, the phase-space velocities and the collision operator appearing in the $y > 1$ equation, Eq. (8), are generalized.

b. *Generalized Physical Quantities in a Bounce-Averaged Scheme*

The code FPSTEL [3, 4] focusses on ripple-trapped particles and thus on low y values. The assumption $K \simeq \mu B_0$ is legitimate for that purpose.

In the present work, we also compute the parallel current, which implies that we must consider all of velocity space ($0 \leqslant v_{\|} \leqslant v$) and not only low y values ($y \to \infty$ for $v_{\|} \to v$). At first sight it might seem that y is not the best pitch-angle variable to describe toroidally blocked and passing particles, for which it is very large (even running off to infinity for particles with $v_{\|} \simeq v$). On the other hand, y is convenient to describe ripple-trapped particles and their detrapping and trapping dynamics. Since the bs current originates from the interaction of ripple-trapped particles with the blocked and passing population, it is important to treat the *transitional region* $t - bl - p$ accurately. Therefore, we opt for y as a pitch-angle variable and circumvent the drawback of large y values via a *multi-mesh* numerical method, as described below.

For large y values, μ is not independent of y; the assumption $\mu \simeq K/B_0$ must be dropped. μ as a function of y, obtained from inverting Eq. (3), is

$$\mu = \frac{K}{B_0(2\varepsilon_h y + 1 - \varepsilon_t \cos\theta - \varepsilon_h)}. \tag{33}$$

For $\varepsilon_h \sim 0.05$–0.1, the y dependence makes itself very noticeable from $y \sim 5$–10 on. For much higher y values, μ varies like the reciprocal of y,

$$\mu \simeq \frac{K}{B_0(2\varepsilon_h y)}; \qquad y \text{ very large.} \tag{34}$$

Because ε_t and ε_h are small compared to 1 it is tempting to ignore the $\varepsilon_t \cos\theta$ and ε_h terms in the denominator of Eq. (33), but the θ dependence is required to have the phase-space divergence property $\nabla \cdot \mathbf{v} \equiv 0$ satisfied. The entire expression for μ, Eq. (33) must be used; Eq. (34) can only be employed for scaling purposes.

Although we shall use Eq. (33) for y values larger than unity, for ripple-trapped particles, we use $\mu \simeq K/B_0$. Matching of the quantities at the $y = 1$ boundary is incorporated in the trapping probability.

In this section we shall obtain general expressions, valid for all y values, for the time-averaged quantities present in the kinetic equation. Successively, we shall consider the Jacobian, the radial-drift velocity, the phase-space flows, and the collision operator.

b.1. *The Jacobian.* In terms of the variables (r, θ, E, μ), the Jacobian is read off from the phase-space volume element: $d^3R\, d^3v = Rr(2\pi/m_a^2) \sum_\sigma B/|v_{||}|$. The helical average of $|v_{||}|^{-1}$ is given by the inverse of Eq. (22). The ba Jacobian in (r, θ, E, μ) variables thus is

$$\langle J_\mu \rangle_> = \frac{\langle J_\mu \rangle_<}{2} = \frac{1}{2} rR \frac{2\pi}{m_a^2} B_0 2A' \frac{\sqrt{m_a}}{2(\varepsilon_h \mu B_0)^{1/2}} = \pi r R \left(\frac{B_0}{\varepsilon_h \mu}\right)^{1/2} \frac{A'}{m_a^{3/2}}. \tag{35}$$

To convert $\langle J_\mu \rangle$ to $\langle J_y \rangle$ we need $\partial\mu/\partial y$, computed from Eq. (33):

$$\left.\frac{\partial \mu}{\partial y}\right|_{K,\theta} = \frac{-2\mu^2 \varepsilon_h B_0}{K}. \tag{36}$$

This result leads to a Jacobian, $\langle J_y \rangle = \langle J_\mu \rangle\, |\partial\mu/\partial y|$, given by

$$\langle J_y \rangle_> = \left[\frac{2\pi r R}{m_a^{3/2}} \varepsilon^{1/2} \frac{B_0^{3/2}}{K}\right] (\mu^{3/2} A') = \frac{2\pi r R}{m_a^{3/2}} \varepsilon_h^{1/2} \frac{\mu B_0}{K} (\mu B_0)^{1/2} A'. \tag{37}$$

The y and θ dependences are isolated in the $\mu^{3/2}A'$ factor. From the second expression, it is clear that the Mynick–Hitchon Jacobian, Eq. (17), is retrieved for $\mu B_0 \simeq K$.

b.2. *The radial-drift velocity.* The grad-B and the curvature drifts of the guiding center are represented by $\mathbf{v}_B$. For low β plasmas, $(\hat{B} \cdot \nabla)\hat{B} \equiv \boldsymbol{\kappa} \simeq (\nabla_\perp B)/B$. Hence

$$\mathbf{v}_B \simeq \frac{\hat{B} \times \nabla B}{\omega_c B} (v_{||}^2 + v_\perp^2/2). \tag{38}$$

The magnetic field can be written approximately as $\mathbf{B} = \mathbf{B}_T + \mathbf{B}_P \simeq -B_T \hat{\zeta} + B_P \hat{\theta}$, in flux coordinates. From Eq. (1), $(\nabla B)/B \simeq (\nabla B)/B_0$ is found to be

$$\frac{\nabla B}{B} \simeq -\hat{r}\left(\frac{\cos\theta}{R_0} + \frac{l}{r}\varepsilon_h \cos\eta\right) + \frac{\hat{\theta}}{r}(\varepsilon_t \sin\theta + l\varepsilon_h \sin\eta) + \hat{\zeta}(m\varepsilon_h \sin\eta), \tag{39}$$

where we have set $R \simeq R_0$. With $B \simeq B_T$, we have that $\hat{B} \simeq \hat{\zeta} + \iota\varepsilon_t \hat{\theta}$ (in flux coordinates).

We concentrate on the radial component of $\mathbf{v}_B$. For the type of machine we consider, $\iota \sim 1$ so that $\iota\varepsilon_t$ is small. Therefore, $\hat{B} \simeq -\hat{\zeta}$ so that we obtain

$$\dot{r} \equiv \mathbf{v}_B \cdot \hat{r} \simeq \frac{K + m_a v_{||}^2/2}{qB_0 r} (\varepsilon_t \sin\theta + l\varepsilon_h \sin\eta). \tag{40}$$

The average over a ripple well eliminates the $\sin\eta$ term. Straightforward computation shows that

$$\langle m_a v_{||}^2 \rangle = \frac{I}{\partial I/\partial E|_\mu}, \tag{41}$$

in which I is the bounce-action integral, and the denominator is the bounce time or transit time. This leads to

$$\langle \dot{r} \rangle = \frac{1}{qB_0 r} \left[K + \frac{I}{2\partial I/\partial E|_\mu} \right] \varepsilon_t \sin\theta. \tag{42}$$

From this expression it is clear that the non-ba radial drift velocity, $\dot{r} - \langle \dot{r} \rangle$, is of the same order as $\langle \dot{r} \rangle$, a claim we made above concerning the scaling arguments.

The bounce action I was computed in Ref. [3]:

$$I = m_a \hat{u} L_h A(y), \tag{43}$$

with $\hat{u}$ given in Eq. (23). Upon combining this expression for I with that for τ_b, given in Eq. (29), we obtain the form for $\langle \dot{r} \rangle$ valid for all y values:

$$\langle \dot{r} \rangle = \frac{K}{qB_0 r} \left[1 + \frac{A}{A'} \varepsilon_h \frac{\mu B_0}{K} \right] \varepsilon_t \sin\theta. \tag{44}$$

For low y values, the second term is negligible, and the Mynick-Hitchon [3, 4] form for $\langle \dot{r} \rangle$, Eqs. (11), (12), is recovered. For large y values, on the other hand, $A/A' \sim y$ and $\mu B_0/K \sim 1/(2\varepsilon_h y)$, implying that both terms in Eq. (44) are of the same order.

Since μ, Eq. (33), is $\cos\theta$ dependent, the θ dependence of $\langle \dot{r} \rangle$ is somewhat more complicated than for FPSTEL [3, 4]. Fortunately, Eq. (44) is still an odd function of θ so that its integral over 2π vanishes. As a result, the driving term $\langle \dot{r} \rangle f'_M$ averages to zero over 2π, as needed for particle conservation.

b.3. *The phase-space flow velocities.* The phase-space flow velocities, $\langle \dot{\theta} \rangle_>$ and $\dot{y}_>$, are still given by Eqs. (24) and (25), respectively, with $\hat{u}$ defined in Eq. (23), but with μ now given by Eq. (33). With Eq. (37), we now show that $\partial(\langle J \rangle \langle \dot{\theta} \rangle_>)/\partial\theta$ and $\partial(\langle J \rangle \dot{y}_>)/\partial y$ no longer vanish.

The expressions for $\langle\dot{\theta}\rangle$ and $\dot{y}$ are written out for convenience:

$$\langle\dot{\theta}\rangle_{>} = 2\sigma \frac{\iota}{R}\left(\frac{\varepsilon_h B_0}{m_a}\right)^{1/2} \frac{\sqrt{\mu}}{A'} \tag{45a}$$

$$\dot{y}_{>} = -\sigma \frac{\iota}{R}\left(\frac{\varepsilon_h B_0}{m_a}\right)^{1/2} \frac{\sqrt{\mu}}{A'} \frac{\varepsilon_t}{\varepsilon_h} \sin\theta. \tag{45b}$$

From Eq. (37), $\langle J\rangle_{>} \equiv C\mu^{3/2}A'$, with C the constant factor within the square bracket. Both $\langle J\rangle\langle\dot{\theta}\rangle_{>}$ and $\langle J\rangle\dot{y}_{>}$ are proportional to μ^2.

Straightfoward differentiation (with $R \simeq R_0$) results in

$$\frac{\partial}{\partial y}(\langle J\rangle \dot{y}_{>}) = C\frac{4\iota\sigma}{R}\left(\frac{B_0\varepsilon_h}{m_a}\right)^{1/2}\frac{B_0}{K}\mu^3\varepsilon_t \sin\theta = -\frac{\partial}{\partial\theta}(\langle J\rangle\langle\dot{\theta}\rangle_{>}), \tag{46}$$

so that the divergence condition is indeed satisfied.

Although the divergence property is exactly satisfied analytically, matters are more complicated for the numerical derivatives because of the finite mesh spacings Δy and $\Delta\theta$. As we shall explain in a later section, the numerical expressions for $\langle\dot{\theta}\rangle$ and $\dot{y}$ used in the code differ slightly from Eq. (45) in order to guarantee exactly that $D_y(\langle J\rangle\langle\dot{\theta}\rangle_{>}) + D_\theta(\langle J\rangle\dot{y}_{>}) = 0$. Here D_y and D_θ are the finite difference equivalents of the derivatives.

b.4. *The collision operator.* We first concentrate on a generalized form for the Lorentz operator $\langle C_L(\langle f\rangle)\rangle$, expressed in the y variable. The momentum-restoring terms are considered at the end of the section.

Application of the chain rule in combination with the reciprocal of Eq. (36) and a form for $\partial I/\partial E|_\mu = (I/2\varepsilon_h\mu_0)(A'/A)$, derived from Eqs. (29), (43), and (23), to the averaged Lorentz operator, Eq. (28), gives

$$\begin{aligned}\langle C_L(\langle f\rangle)\rangle &= \left(\frac{2\mu\varepsilon_h B_0}{I}\frac{A}{A'}\right)\frac{\nu_D}{B}\left(\frac{K}{2\mu^2\varepsilon_h B_0}\right)\frac{\partial}{\partial y}\left(\frac{IK}{2\mu\varepsilon_h B_0}\frac{\partial\langle f\rangle}{\partial y}\right)\\ &= \frac{\nu_D}{B}\frac{K^2}{2\varepsilon_h B_0}\frac{A}{A'I\mu}\frac{\partial}{\partial y}\left(\frac{I}{\mu}\frac{\partial\langle f\rangle}{\partial y}\right).\end{aligned} \tag{47}$$

From Eqs. (43) and (23), $I/(A\sqrt{\mu})$ is independent of y, hence

$$\langle C_L(\langle f\rangle)\rangle = \frac{\nu_D}{B}\frac{K^2}{2\varepsilon_h B_0}\frac{1}{\mu^{3/2}A'}\frac{\partial}{\partial y}\left(\frac{A}{\sqrt{\mu}}\frac{\partial\langle f\rangle}{\partial y}\right) \simeq \frac{\nu_D}{2\varepsilon_h}\frac{K^2}{\mu^2 B_0^2}\frac{\sqrt{\mu}}{A'}\frac{\partial}{\partial y}\left(\frac{A}{\sqrt{\mu}}\frac{\partial\langle f\rangle}{\partial y}\right). \tag{48}$$

For low y values, $\mu \simeq K/B_0$, and the operator reduces to the form used in FPSTEL [3, 4], Eq. (30). For $y \gg 1$, we find that both terms in $\partial/\partial y(A\mu^{-1/2}) = A\mu^{-1/2}[A'/A + \varepsilon_h\mu B_0/K]$ contribute equally, since $A'/A \sim \varepsilon_h\mu B_0/K \sim 1/y$.

To ensure particle conservation, the kinetic equation and also the Lorentz part of the collision operator must be written in conservation form, i.e., as a divergence.

To do so with Eq. (48), we isolate the $\mu^{3/2}A'$ factor in $\langle J\rangle$, Eq. (37), within the first $\partial/\partial y$ operator,

$$\langle C_L(\langle f\rangle)\rangle = \left(\frac{\nu_D}{2\varepsilon_h}\right)\frac{K^2}{B_0^2}\frac{1}{\langle J\rangle}\frac{\partial}{\partial y}\left[\langle J\rangle\frac{(A/A')}{\mu^2}\frac{\partial\langle f\rangle}{\partial y}\right]$$

$$= \frac{1}{\langle J\rangle}\frac{\partial}{\partial y}\left\{\langle J\rangle\left[\nu_h\left(\frac{K}{\mu B_0}\right)^2\frac{A}{A'}\frac{\partial\langle f\rangle}{\partial y}\right]\right\}, \tag{49}$$

where $\nu_h \equiv \nu_D/(2\varepsilon_h) \equiv \nu_\perp(v)/(4\varepsilon_h)$. For $\nu_\perp(v)$, the formulae of Ref. [9] were used.

The momentum-restoring terms in the collision operator are of the form [26, 5]

$$u_{a1}\text{ restoring term} \sim \nu_{||}u_{a1}(v) \tag{50a}$$

$$r_{ba}\text{ restoring term} \sim \nu_{||}r_{ba}; \tag{50b}$$

$u_{a1}(v)$ and r_{ba} are $\nu_{||}$ moments of f over pitch angle and all of velocity space, respectively.

For ripple-trapped particles, the u_{a1} and r_{ba} terms vanish. After the integrations, $u_{a1}(v)$ is a speed-dependent function and r_{ba} is merely a number. Both are insensitive to the sign of $\nu_{||}$. Hence, since $\langle\nu_{||}\rangle = 0$ for ripple-trapped particles, the ba of the momentum-restoring terms vanishes identically.

Therefore, the Lorentz part alone is momentum conserving in the ba formalism, for ripple-trapped particles. Even our approximate ba Lorentz operator, $\langle C_L(\langle f\rangle)\rangle$, conserves parallel momentum exactly, since it is independent of $\text{sign}(\nu_{||})$ for trapped particles. The u_{a1} and r_{ba} restoring terms for blocked and passing particles are computed in our approach as

$$\langle u_{a1}\text{ restoring term}\rangle \sim \langle\nu_{||}\rangle\int d\Omega\langle\nu_{||}\rangle\langle f_1^a\rangle \tag{51a}$$

$$\langle r_{ba}\text{ restoring term}\rangle \sim \langle\nu_{||}\rangle\int d^3v\langle\nu_{||}\rangle\langle f_1^b\rangle. \tag{51b}$$

Here $d\Omega$ is the differential solid angle in velocity space: $d\Omega = d^3v/(v^2\,dv) = 2\pi\,d\nu_{||}/v$.

With regard to particle conservation, these restoring terms are proportional to $\sigma = \text{sign}(\nu_{||})$; the integrals are independent of σ, because the integration over $\nu_{||}$ has been performed. These terms appear with the opposite sign in the equations for the forward and backward distribution functions. Integration over all of velocity space of these momentum-restoring terms gives zero; they are thus momentum conserving.

V. Numerical Implementation of the FLOCS Code

To numerically solve the kinetic equations using the generalized phase-space flows and collision operator, discussed in the previous section, there are some

crucial issues that ought to be examined carefully. First, as alluded to above, the *divergence condition* must be satisfied exactly numerically. Second, an economical code must resort to a *multi-mesh method* in the variable y. This in turn requires careful consideration of the divergence condition at the mesh transitions. Finally, we propose a cure for the artificial jump in the backwards distribution function $\langle f_b \rangle$ obtained with FPSTEL [3, 4]. For this purpose, the boundary conditions at $y = 1$ are revisited.

In FLOCS, the same explicit numerical scheme as in FPSTEL has been adopted. This was done in part for pragmatic reasons, because FPSTEL is an established code, which was the starting point for our work. Furthermore, the explicit time-advancing scheme permits the study of the time evolution of the plasma. For time-independent problems, an implicit scheme could be used as well, in which the coupling between the ion and electron species (via the momentum-restoring terms) is taken care of iteratively. It should be noted, however, that because of the still applicable divergence condition, $\nabla \cdot \mathbf{v} \equiv 0$, the set up of the meshes, as well as their overlap, and the "in principle" numerical form of the equations and boundary conditions remains effectively unchanged.

In the first subsection, a, the divergence question will be addressed. Stability and the multi-mesh method are treated in subsections b and c, respectively. We end this section in subsection d by considering the $y = 1$ boundary.

a. *The Numerical Divergence Condition*

Satisfying the divergence condition for $y > 1$, $\partial/\partial\theta(\langle J \rangle \langle \dot{\theta} \rangle_>) + \partial/\partial y(\langle J \rangle \dot{y}_>) = 0$, does not automatically guarantee that its finite-differenced equivalent vanishes as well, because of the finite mesh spacings Δy and $\Delta\theta$. To resolve this issue, appropriate new numerical flows, $\langle \dot{\theta}_n \rangle_>$ and $\dot{y}_{n>}$ are derived, which approach the analytic forms $\langle \dot{\theta} \rangle_>$ and $\dot{y}_>$ in the limit $\Delta\theta, \Delta y \to 0$.

To find these new numerical flows, we first rewrite the analytic divergence condition in terms of what we shall refer to as (phase-space) "fluxes," $\hat{\gamma}^\theta_> \equiv \langle J \rangle \langle \dot{\theta} \rangle_>$ and $\hat{\gamma}^y_> \equiv \langle J \rangle \dot{y}_>$:

$$\frac{\partial}{\partial\theta}\hat{\gamma}^\theta_> + \frac{\partial}{\partial y}\hat{\gamma}^y_> = 0. \tag{52}$$

(These $\hat{\gamma}$'s are in fact "fluxes" for a distribution function of unity.) Since $\hat{\gamma}^\theta_>$ and $\hat{\gamma}^y_>$ have a two-dimensional divergence of zero, they must be derivable from a *streaming function* Λ. We have

$$\hat{\gamma}^\theta_> = \partial\Lambda/\partial y, \tag{53a}$$

$$\hat{\gamma}^y_> = -\partial\Lambda/\partial\theta. \tag{53b}$$

Λ is obtained from integrating Eqs. (53). Combining the constant factors in $\langle J \rangle_>$, Eq. (37), and in $\langle \dot{\theta} \rangle_>$, Eq. (45a), into one symbol c, the differential equations for Λ become

$$\frac{\partial \Lambda}{\partial y} = c\mu^2, \tag{54a}$$

$$\frac{\partial \Lambda}{\partial \theta} = c\frac{\varepsilon_t}{2\varepsilon_h}\sin\theta\,\mu^2. \tag{54b}$$

Integration of the first equation with respect to y gives

$$\Lambda = -c\frac{K}{2\varepsilon_h B_0}\mu + h(\theta), \tag{55}$$

where we used Eq. (33). If we now take the θ derivative of Eq. (55) and equate it to Eq. (54b) we can determine h: all terms except that involving h cancel, and we find

$$\frac{\partial h}{\partial \theta} = 0 \Rightarrow h = \text{const.} \tag{56}$$

Therefore, h is irrelevant for the stream function Λ, which is

$$\Lambda = -c\frac{K}{2\varepsilon_h B_0}\mu. \tag{57}$$

Before writing the explicit expressions for $\langle \dot{\theta}_n \rangle_>$ and $\dot{y}_{n>}$ we introduce a notation for the mesh points. The index specification of a y mesh point is denoted by iy; a θ mesh point is referred to as ip ("p" for poloidal angle).

The *numerical flows* $\langle \dot{\theta}_n \rangle_>$ and $\dot{y}_{n>}$ are to be found from the finite-difference analog of Eq. (53):

$$\langle \dot{\theta}_n \rangle_> \equiv \frac{1}{\langle J \rangle} D_y \Lambda \tag{58a}$$

$$\dot{y}_{n>} \equiv -\frac{1}{\langle J \rangle} D_\theta \Lambda. \tag{58b}$$

Performing this numerical derivative from Eq. (57), we obtain

$$\langle \dot{\theta}_n \rangle_> (iy, ip) = -\frac{1}{\langle J(iy, ip) \rangle}\frac{c}{2\Delta y}\frac{K}{2\varepsilon_h B_0}[\mu(iy+1, ip) - \mu(iy-1, ip)] \tag{59a}$$

$$\dot{y}_{n>}(iy, ip) = \frac{1}{\langle J(iy, ip) \rangle}\frac{c}{2\Delta\theta}\frac{K}{2\varepsilon_h B_0}[\mu(iy, ip+1) - \mu(iy, ip-1)]. \tag{59b}$$

As $\Delta y \to 0$ and $\Delta\theta \to 0$, these reduce to the analytic forms, Eqs. (45).

If we set $\hat{c} = cK/(2\varepsilon_h B_0)$, we can write for the numerical derivatives of $\hat{\dot{\gamma}}^{\theta}_{n>}$ and $\hat{\dot{\gamma}}^{y}_{n>}$:

$$D_\theta(\langle J\rangle\langle\dot\theta_n\rangle_>)_{iy,ip} = -\frac{\hat c}{4\Delta y\,\Delta\theta}[\mu(iy+1,ip+1)-\mu(iy+1,ip-1) - \mu(iy-1,ip+1)+\mu(iy-1,ip-1)] \tag{60a}$$

$$D_y(\langle J\rangle\dot y_{n>})_{iy,ip} = \frac{\hat c}{4\Delta y\,\Delta\theta}[\mu(iy+1,ip+1)-\mu(iy-1,ip+1) - \mu(iy+1,ip-1)+\mu(iy-1,ip-1)]. \tag{60b}$$

These sum to zero, so the numerical divergence condition is satisfied exactly:

$$D_\theta(\hat y^\theta_{n>}) + D_y(\hat y_{n>}) \equiv 0. \tag{61}$$

b. *Numerical-Stability Analysis*

Stability of an explicit numerical scheme requires that the numerical propagation speed $V_{\rm num} \equiv \Delta x/\Delta t$, in which Δx is a mesh spacing in the x direction, must be greater than the speed at which the physical process travels across the mesh.

We have two kinds of physical "flow" processes to consider. First there are the phase-space flows $\langle\dot\theta\rangle$ and $\dot y$. These flows increase gradually with y, to reach an asymptotic value for $y\to\infty$, when $v_{||} = v = \sigma(2K/m_a)^{1/2}$, and $\langle\dot\theta\rangle_> = (\iota/R)v$ and $\dot y_> = -\varepsilon_t/(2\varepsilon_h)\langle\dot\theta\rangle_> \sin\theta$. The conditions for numerical stability over the mesh are

$$\Delta y > \Delta t\,\dot y_> \qquad \text{or} \qquad \Delta t < \frac{\Delta y}{\dot y_>} \tag{62a}$$

$$\Delta\theta > \Delta t\langle\dot\theta\rangle_> \qquad \text{or} \qquad \Delta t < \frac{\Delta\theta}{\langle\dot\theta\rangle_>}. \tag{62b}$$

These prescriptions are fairly easily satisfied for reasonable mesh sizes, $\Delta\theta$ and Δy, and time step Δt. For given mesh spacings $\Delta\theta$ and Δy, the code estimates the maximum time step Δt according to Eq. (62). The actual timestep is down by a factor α from that prescribed by Eq. (62). α is a "safety factor" and its value can be chosen at will; presently, a value $\alpha\sim 3$ is used. The stability conditions for phase-space flows are more stringent for electrons than for ions. This is because the flows of the former are a factor $(m_i/m_e)^{1/2} \simeq 43$ larger than for ions.

The phase-space flows $\langle\dot\theta\rangle$ and $\dot y$ for $y<1$ are smaller than those for $y>1$, and do not enter the stability considerations.

The second physical flow process is a diffusive flow. For a typical diffusion equation with diffusion coefficient D, the stability criterion requires that

$$\Delta x > (D\,\Delta t)^{1/2} \qquad \text{or} \qquad \Delta t < (\Delta x)^2/D. \tag{63}$$

As we shall demonstrate momentarily, these conditions force us to use a multi-mesh method in the y variable.

$$\simeq 4\varepsilon_h \nu_D \left[y^3 \frac{\partial^2 \langle f \rangle}{\partial y^2} + y^2 \frac{\partial \langle f \rangle}{\partial y} \right]. \tag{64}$$

The coefficient of the second derivative is the diffusion coefficient in velocity space:

$$D_y \simeq (4\varepsilon_h \nu_D)\, y^3. \tag{65}$$

To satisfy the stability criterion, Eq. (63), we must guarantee that

$$\Delta t < \frac{(\Delta y)^2}{4\varepsilon_h \nu_D} \frac{1}{y^3} \tag{66}$$

for a given mesh space Δy. Alternatively,

$$\Delta y > 2(\varepsilon_h \nu_D)^{1/2} \sqrt{\Delta t}\; y^{3/2} \tag{67}$$

for a chosen time step Δt.

Adjusting the time step Δt to accommodate a given Δy proves to be detrimental. Since the kinetic equation is solved by relaxation until $\partial \langle f \rangle / \partial t \to 0$, the total run time T_{tot} is fixed by the physical relaxation processes, i.e., $T_{\text{tot}} \sim 1/\nu_\perp$. On the other hand, we need a rather fine mesh for ripple-trapped and toroidally-blocked particles up to $y \sim 3$ to describe the trapping/detrapping physics accurately. Such a high resolution (i.e., small Δy) combined with the y^{-3} variation for large y values would oblige us to take extremely small time steps. For an externally imposed T_{tot}, this would lead to an impactically large number of time steps.

To reconcile the high resolution needed for low y values with the required large values of y necessary to compute the $v_{||}$ moments of $\langle f \rangle$ sufficiently accurately, we have devised a multi-mesh method in y. A first mesh runs from $y = 0$ to $y \simeq 3$, a second from $y \simeq 3$ to $y \simeq 5$, etc. From one mesh to the next, the mesh spacing is doubled. The details of this multi-mesh approach are deferred to the next section; here we concentrate on justifying why such a method works.

Because of the y^3 coefficient, the collision operator, Eq. (64b), rapidly becomes dominant in the kinetic equation for large y values. It assumes the responsibility for balancing the driving term $\langle \dot{r} \rangle f'_M$ (see Eq. (8)):

$$4\varepsilon_h \nu_D\, y^2 \frac{\partial}{\partial y} \left(y \frac{\partial \langle f \rangle}{\partial y} \right) \simeq \langle \dot{r} \rangle f'_M, \qquad y \gg 1. \tag{68}$$

Two integrations lead to

$$\langle f\rangle \simeq \left(\frac{\langle \dot{r}\rangle f'_M}{4\varepsilon_h v_D}\right)\frac{1}{y} + c_1 \ln y + c_2, \qquad y \gg 1, \tag{69}$$

where c_1 and c_2 are integration constants. A physical solution for $\langle f\rangle$ must be finite for $y \to \infty$ or, equivalently, $v_{||} \to v$. $\langle f(y \to \infty)\rangle$ describes very passing particles. Consequently, c_1 must be chosen equal to zero. Hence, we conclude that

$$\langle f(y \gg 1)\rangle = \left(\frac{\langle \dot{r}\rangle f'_M}{4\varepsilon_h v_D}\right)\frac{1}{y} + c_2. \tag{70}$$

This equation states that $\langle f\rangle$ levels off to a constant value, c_2, for $y \to \infty$. It also indicates that the change in $\langle f\rangle$ with y, $\partial\langle f\rangle/\partial y$, is quite small for large y values. This observation permits us to use a coarse mesh for large y.

A next question to be answered is, how large are the y values that we have to consider in practice? As will be recalled, we have to consider large y's to be able to compute the $v_{||}$ moments of $\langle f\rangle$, which involve integration over all of velocity space. For each of these, the y integration runs (in principle) from $y = 1$ to $y \to \infty$:

$$\int d^3v \langle v_{||}\rangle \langle f\rangle = \sum_\sigma \int_0^\infty dK \int_1^\infty dy \frac{\langle J\rangle}{rR} |\langle v_{||}\rangle| \langle f\rangle. \tag{71}$$

We recall that $\langle J\rangle \propto \mu^{3/2}A'$ and $|\langle v_{||}\rangle| \propto \mu^{1/2}/A'$. Therefore, as far as the y integration is concerned,

$$\int d^3v \langle v_{||}\rangle \langle f\rangle \sim \int_1^\infty dy\, \mu^2 \langle f\rangle \sim \int_1^\infty \frac{dy \langle f\rangle}{(1+2\varepsilon_h y)^2}. \tag{72}$$

Here we replaced μ by $(K/B_0)(1+2\varepsilon_h y)^{-1}$, dropping the small $\varepsilon_t \sim \varepsilon_h$ terms in Eq. (33). Since for large y values, $\langle f\rangle$ can roughly be considered as a constant, according to Eq. (70), it is easily demonstrated from Eq. (72) that replacing the upper limit $y \to \infty$ by $y \simeq y_{\max} \sim 100$ leads to errors of 5 and 10% for ε_h values of 10 and 5%, respectively. Since $\simeq 10\%$ is the overall accuracy of this computation, we shall take $y_{\max} \sim 100$.

Our strategy should be clear. We wish to keep y as a pitch-angle variable because y is very convenient to describe ripple-trapped and toroidally-blocked particles. Moreover, it is desirable to keep the mesh linear at low y values to see more readily the y dependence of $\langle f\rangle$. The drawback of having to deal with large y values when the integrals are performed is circumvented by a multi-mesh method. We start with a fine mesh for low y values and introduce gradually coarser meshes for larger y values. The code FLOCS is capable of handling any number of meshes desired. For the results to be reported in the next section, we used seven interlinked meshes.

As an alternative to a multi-mesh approach one might consider using $\log y$ or $1/y$ or even μ as a variable for large y values. Although μ is an appropriate variable

for passing particles, it is inconvenient to use it for ripple-trapped particles. Using y for low y values and μ for large ones is a difficult task in that matching a linear y mesh onto a μ mesh is rather complicated. As far as the log y and $1/y$ options are concerned, it is not clear at what y value a transition from y to the alternative should be considered. It is our intuitive feeling that a linear y mesh should be used up to $y \sim 5$–10. However, at such y values one is already forced to use a Δy spacing which is too coarse for the $y \sim 1$ region, in order to meet reasonable CPU considerations. Hence, a multi-mesh approach seems to be the most clear-cut way to resolve this issue. Once the mechanics for the multi-mesh method were incorporated in FLOCS, it proved to be a very flexible tool (depending on where the mesh transitions are chosen, FLOCS can resolve certain regions of phase space better than others; because of the free choice of the mesh transitions, it seems to be more flexible than a prescribed functional dependence of the mesh spacing).

We arrived at a value $y_{\max} \sim 100$ by considering the $v_{||}$ moment of $\langle f \rangle$ in Eq. (72). FLOCS also computes the radial fluxes, which are proportional to a velocity-space integral $\int d^3v \langle \dot{r} \rangle f'_M$. However, for the radial flux, only the low y values contribute significantly. The bulk of the transport is due to ripple-trapped particles ($y < 1$), a small fraction is contributed by toroidally-blocked particles ($y < y_{tp}$), and a generally negligible amount originates with passing particles. For the radial flux a maximum y value, $y_{\max} \sim 3$, is sufficient for the ε_h and ε_t values we consider.

For each mesh point of all submeshes, the maximum timestep Δt is evaluated and the smallest of these is used by the code (again after reduction by a "safety factor" $\alpha \sim 3$).

It is to be expected that in the high collisionality regime, the maximum Δt will be obtained from the diffusive-flow constraint, Eq. (66). For low ν regimes, the phase-space flow condition, Eq. (62), plays a significant role, especially at the mesh points where Δy is small. Recall that the $\Delta\theta$ spacing is constant (and small) everywhere. For low collision frequencies the timestep limitation could therefore be caused by the θ-stability condition, Eq. (62b).

c. *Structure of the* (θ, y) *Mesh*

The grid used to cover the (θ, y) plane, $-\pi < \theta \leqslant \pi$ and $0 \leqslant y < 100$, consists of a single evenly spaced θ mesh and N different interlinked y meshes. From a mesh covering low y values to the next one representing higher y values, the Δy mesh spacing is doubled. The results presented in the next section are obtained with mesh spacings $\Delta\theta \sim 2\pi/20$–$2\pi/10$ and $(\Delta y)_{\text{finest mesh}} \sim 0.05$–$0.1$. We used seven interlinked meshes with respective maximum y values 3, 5, 8, 16, 30, 50, 90.

In the middle of each mesh, the finite differencing is done as usual, taking into account the proper mesh spacings for that mesh. Caution is needed at the connection of two meshes, however. In order to propagate information up and down the y meshes, quantities at one end of one mesh must be expressed in terms of those of the neighboring mesh, because the ubiquitous divergence condition must be satisfied.

We first consider the bottom y mesh ranging from $y=0$ to about $y=3$. In Fig. 4, we show its position in relation to $y=1$ as well as the top of the mesh. We use the convention (as in the original code FPSTEL) that the iy index increases with decreasing y value. Hence, the Δy in the code is a negative number, represented by Δy_n (the index n refering to numerical). (For the poloidal angle both θ and ip increase in the same direction.) The mesh is positioned symmetrically about the $y=1$ boundary: the first mesh point above $y=1$ has a y value $y=1+|\Delta y_n|/2$; the first point below $y=1$ is $y=1-|\Delta y_n|/2$.

The labeling of the mesh points around $y=1$ is self-explanatory. Point $iyeq1$ is the iy value (immediately above) where y equals 1; $iy1p1=iyeq1+1$ and $iy1m1=iyeq1-1$. In what follows, the extra (1) between parentheses specifies that it concerns the first mesh.

Near the top of the mesh we have the meshpoint $iyu(1)$ indicating the "upper" point of the first mesh. $iyuf(1)$ is the so-called "final upper" point. The y value $yupper(1)$ is the top y value for the first mesh. For the results in the next section, $yupper(1)=3$.

In order to set the reference for the finite differencing near mesh transitions (to be discussed momentarily), we first consider the differencing equation for point

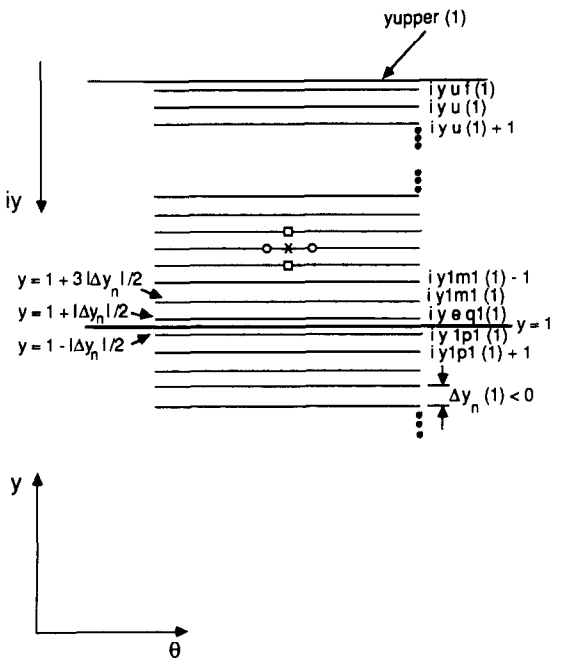

FIG. 4. The first y mesh, centered about $y=1$.

(iy, ip) of Fig. 4. We shall concentrate on the flow terms of the kinetic equation in conservation form [3]:

$$\frac{\partial \langle f \rangle}{\partial t} = -\frac{1}{\langle J \rangle}\left[\frac{\partial}{\partial \theta}(\langle J \rangle \langle \dot{\theta} \rangle \langle f \rangle) + \frac{\partial}{\partial y}(\langle J \rangle \dot{y} \langle f \rangle)\right] + \text{remainder} \tag{73}$$

which becomes, after finite differencing,

$$\langle \Delta f(iy, ip) \rangle = -\left\{\frac{[\hat{\gamma}^{\theta}_{n>}(iy, ip+1)\langle f(iy, ip+1)\rangle - \hat{\gamma}^{\theta}_{n>}(iy, ip-1)\langle f(iy, ip-1)\rangle]}{2\Delta\theta}\right.$$
$$\left. + \frac{[\hat{\gamma}^{y}_{n>}(iy+1, ip)\langle f(iy+1, ip)\rangle - \hat{\gamma}^{y}_{n>}(iy-1, ip)\langle f(iy-1, ip)\rangle]}{2\Delta y_n(1)}\right\}$$
$$\times \{\Delta t/\langle J(iy, ip)\rangle\} + \text{remainder}. \tag{74}$$

Here *remainder* stands for the sum of the (negative) collision operator and the driving term (multiplied by Δt). The point (iy, ip) is represented by the cross "$\times$" in Fig. 4. The θ differencing is done between the circles, and the y differencing is performed on the squares.

In Fig. 5 we show the interlink between two meshes. The solid lines belong to the "lower" mesh covering lower y values. The dashed lines describe higher y values. Since the first mesh for untrapped particles (see Fig. 4) runs over the indices $iyuf(1)$ to $iyeq1(1)$, we have labeled all higher-order meshes analogously: they run from

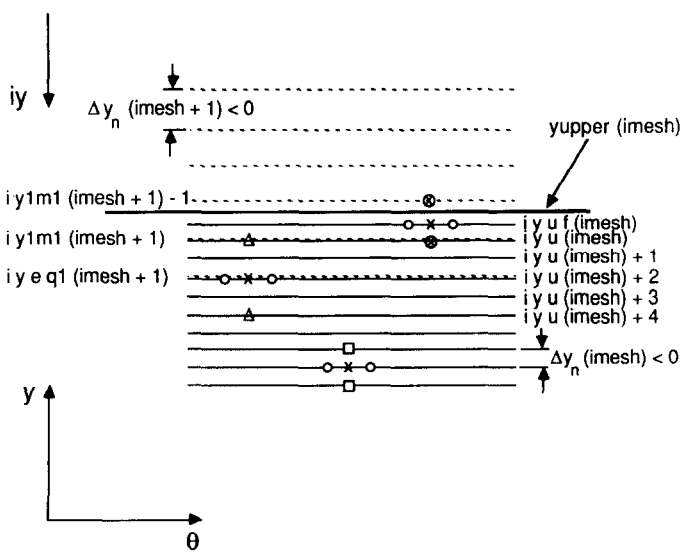

FIG. 5. Transition between y meshes, *imesh* (solid), and *imesh* + 1 (dashed).

iyuf(*imesh*) to *iyeq*1(*imesh*), where *imesh* is an additional index to label the "order" of the mesh. On the right-hand side of Fig. 5, the indices label the top of the mesh *imesh*, represented by solid lines. On the left, the indices refer to the bottom of the dashed mesh, *imesh* + 1.

Two neighboring meshes must overlap to a certain extent, as shown in Fig. 5. This is required so as to be able to propagate information from one mesh to the other, and to have the divergence condition satisfied exactly at those transitions. (The complication arises from the different mesh spacings at the transition.)

To have information travel downward, the y differencing at the top of the mesh at point *iyuf*(*imesh*) is obtained from the two points of the dashed mesh, represented by the circled crosses in Fig. 5 and labeled *iy*1*m*1(*imesh* + 1) and *iy*1*m*1(*imesh* + 1) − 1. The θ differencing is as usual. Instead of Eq. (74) we have thus for the y differencing at point (*iyuf*(*imesh*), *ip*)

$$\begin{aligned}
&\langle \Delta f(iyuf(imesh), ip)\rangle \\
&= -\{[\hat{\gamma}^{\theta}_{n>}(iyuf(imesh), ip+1)\langle f(iyuf(imesh), ip+1)\rangle \\
&\quad -\{\hat{\gamma}^{\theta}_{n>}(iyuf(imesh), ip-1)\langle f(iyuf(imesh), ip-1)\rangle]/2\Delta\theta \\
&\quad +[\hat{\gamma}^{y}_{n>}(iy1m1(imesh+1), ip)\langle f(iy1m1(imesh+1), ip)\rangle \\
&\quad -\hat{\gamma}^{y}_{n>}(iy1m1(imesh+1)-1, ip)\langle f(iy1m1(imesh+1)-1, ip)\rangle]/\Delta y_n(imesh+1)\} \\
&\quad \times\{\Delta t/\langle J(iyuf(imesh), ip)\} + \text{remainder.}
\end{aligned} \tag{75}$$

Thus as is clear from the equation, the rate of change of $\langle f\rangle$ at *iyuf*(*imesh*) is determined by differencing the (near) bottom points of the higher-order mesh, *imesh* + 1.

As will be recalled, the θ "fluxes" $\hat{\gamma}^{\theta}_{n>}$, are obtained from the y differencing of the stream function Λ (effectively μ). At interior points of a mesh the y differencing is done using neighboring mesh points of the same mesh. However, in order to satisfy the divergence condition at the top of the mesh, the θ "flux" $\hat{\gamma}^{\theta}_{n>}(iyuf(imesh))$ must be computed from differencing the stream function at points of mesh (*imesh* + 1). We have now in comparison to Eq. (59a)

$$\begin{aligned}
&\hat{\gamma}^{\theta}_{n>}(iyuf(imesh), ip) \\
&\quad = \frac{-c(K/2\varepsilon_h B_0)}{\Delta y_n(imesh+1)}[\mu(iy1m1(imesh+1), ip) - \mu(iy1m1(imesh+1)-1, ip)].
\end{aligned} \tag{76}$$

Equation (76) cannot be utilized for the very last mesh, however. How the boundary condition at the point *iyuf*(*Nmesh*) is applied will be discussed in the next section.

To make information move upward in y, an analogous "mixed" differencing is used at the bottom of a mesh. The y differencing at the bottom point of mesh

$(imesh+1)$, namely at $iyeq1(imesh+1)$, is obtained from the points $iyu(imesh)+4$ and $iyu(imesh)$, represented by the triangles in Fig. 5. The mesh spacing appearing in the denominator is $4\Delta y_n(imesh)$. The θ differencing is as usual, but the θ "flux", $\hat{\gamma}^{\theta}_{n>}(iyeq1(imesh+1), ip)$, is constructed from differencing at the "triangle mesh points" of mesh *imesh*. All of the above holds for all *iyeq1*'s except $iyeq1(1)$, since there the boundary conditions at $y=1$ apply, which will be treated in the next section.

d. *Boundary Conditions at $y=1$ and at the Top of the Mesh*

Because in our present work the $\langle\dot{\theta}\rangle_>$ and $\dot{y}_>$ flows are dependent on θ, we must pay special attention to the boundary conditions at $y=1^+$ and at the top of the mesh, at $iyuf(Nmesh)$, where *Nmesh* is the last y mesh. As part of considering the boundary condition at $y=1$, we shall propose a remedy to erase the artificial jump in $\langle f_b\rangle$ imposed on FPSTEL [3, 4]. Also, we shall adjust the θ flows for $y=1^-$ to make sure that the boundary condition is better satisfied than was the case in FPSTEL. For completeness, we mention that the boundary condition at the very bottom of the mesh, at $y=0$, is left unchanged, compared to Refs. [3, 4].

At the very last y mesh point, $iy=iyuf(Nmesh)$, there is no next iy point to do the y differencing. Mynick and Hitchon [1, 2] resolved this difficulty by making particles flowing out of the top mesh at (θ, y_{uf}) immediately reappear at the symmetric point $(-\theta, y_{uf})$. For y_{uf} large enough, little physics is lost. Because our $\hat{\gamma}$ "fluxes" are θ and y dependent, matters are a bit more subtle than in FPSTEL [3, 4]. Instead of Eq. (75), a different equation is needed: rather than using a point $(iyuf(Nmesh)-1, ip)$, which does not exist, the point $(iyuf(Nmesh), iq)$ is used, where iq denotes the symmetric point about $\theta=0$. To guarantee that the divergence condition is satisfied, the θ "fluxes" must again be adjusted, since the y differencing is in fact now done over one mesh spacing. We observe that

$$\mu(iy, ip+1)-\mu(iy, ip-1)=-[\mu(iy, iq+1)-\mu(iy, iq-1)], \tag{77}$$

since both these differences are odd in θ (their numerator goes like $\sin\theta\cos\theta$). The expression for $\hat{\gamma}^{\theta}_{n>}(iyuf(Nmesh), ip)$ is

$$\hat{\gamma}^{\theta}_{n>}(iyuf(Nmesh), ip) = \frac{-c(K/2\varepsilon_h B_0)}{\Delta y_n(Nmesh)}[\mu(iyu(Nmesh), ip)-\mu(iyuf(Nmesh), ip)]. \tag{78}$$

The equations given so far, can all be written for *forward* and *backward* moving particles. The general symbol $\hat{\gamma}^{\theta}_{n>}\equiv\langle J\rangle_>\langle\dot{\theta}_n\rangle_>$ can be replaced by $\hat{\gamma}^{\theta}_f$ or $\hat{\gamma}^{\theta}_b$ according to which flux is of concern, and similarly for the y "fluxes." It is a matter of convention which flows are taken to be positive. If, say, the forward flow is positive, then according to Eq. (24), the backward flow will be negative. (In Eq. (55), $\sigma=\text{sign}(v_{||})$ is buried in the constant c.) We shall argue momentarily that forward and backward fluxes should not merely be each other's negatives, but should also have a slight imbalance in magnitude.

We now take a closer look at the region near $y=1$. Near the $y=1$ boundary, three kinds of particles are involved, *trapped* (t), *forward* (f), and *backward* (b). The FPSTEL boundary conditions (bc's) are discussed in detail in Refs. [3, 4].

A detailed examination of the bc's used in FPSTEL [3, 4] shows that they do not exactly satisfy the divergence condition. For the bc at point $y=1-\Delta y/2$ (for the trapped particles) the problem is easily resolved when it is recognized that it involves finite differencing across only one mesh spacing: A' at that meshpoint should also be differenced across one mesh spacing, instead of across two as done usually.

At the entrapping side at $y=1+\Delta y/2$, matters are a bit more subtle. For forward particles, we have the equation

$$0 = D_\theta \hat{\gamma}_f^\theta(\theta, 1+\Delta y/2) + [\hat{\gamma}_t^y(\theta, 1-\Delta y/2) - \hat{\gamma}_b^y(\theta, 1+\Delta y/2) - \hat{\gamma}_f^y(\theta, 1+3\Delta y/2)]/2\Delta y. \tag{79}$$

In FPSTEL [3] both "fluxes" $\hat{\gamma}_f^y$ and $\hat{\gamma}_b^y$ are independent of y, and are each other's negative. Consequently, the last two terms in Eq. (79) cancel. Also, $\hat{\gamma}_f^\theta$ is independent of θ, Eq. (26), setting the D_θ term in Eq. (79) equal to zero. Therefore, we must conclude that $\hat{\gamma}_t^y(\theta, 1-\Delta y/2) \equiv p_{ft}\hat{\gamma}_f^y(\theta, 1+\Delta y/2)$ survives, leaving Eq. (79) with a non-vanishing right-hand side. (The trapping probability p_{ft} was discussed above in Eq. (31).)

Investigation of the bc for backward-moving particles, leads to the same conclusion.

This failure to satisfy the divergence condition is because of the original inconsistency in FPSTEL [3] which forced the authors to lower the backwards distribution function artificially. The bc's at $y=1+\Delta y/2$ are not satisfied because the definition of the trapping probability p_{ft}, Eq. (31), is incompatible with the fact that the y fluxes $\hat{\gamma}_b^y$ and $\hat{\gamma}_f^y$ are merely each other's negatives. Setting $\hat{\gamma}_b^y = -\hat{\gamma}_f^y$ does not allow a fraction of the forward flux to become entrapped.

We conjecture that the forward flux should be a factor $(1-p_{ft})^{-1}$ larger than the backward flux. Making the forward y flux larger than the backward y flux seems to be connected with the neglect of the poloidal cross-field drifts for untrapped particles. It is not clear, however, to which factor in $\hat{\gamma}^y = \langle J \rangle \dot{y}$ it should be attributed.

Intuitively, we would argue that this $(1-p_{ft})$ factor adjustment should be ascribed to the Jacobian, because there is slightly less phase space available to backward particles than to forward moving particles, since the latter have access to a $|\mathbf{B}|$ window which can permit them to become trapped. The reason why this is not reflected in the averaged Jacobian is because we always compute the time averages as $dl/v_{\|}$ averages, neglecting the small cross-field drifts, whereas it is precisely the deviation from field lines due to these drifts that makes entrapping possible.

On the other hand, one might claim that the cross-field poloidal drifts should have been included in the $\langle \dot{\theta} \rangle_>$ flows in addition to the parallel free-streaming part, which in turn determine the $\dot{y}_>$ flows. This observation was made in Ref. [3].

Although this is at first sight a logical explanation, it only works for one sign of the radial electric field (whose $E \times B$ poloidal flow adds to the poloidal projection of the free streaming of the forward particles). Furthermore, experience with the code has shown us that the precise value of the $\langle \dot{\theta} \rangle_>$ flow is not crucial as long as $|\dot{y}_f| = |\dot{y}_b|/(1 - p_{ft})$.

The above discussion as to which factor should be responsible for the adjustment is somewhat academic since in the code the factors always appear combined.

We propose that the forward flux of FPSTEL, $\hat{\gamma}_f^y$, be increased by a factor $(1 - p_{ft})^{-1/2}$ over its value prescribed by Eqs. (24) and (25). The backward flux $\hat{\gamma}_b^y$ should be multiplied by $(1 - p_{ft})^{1/2}$ and thus reduced by a small fraction. With

$$\hat{\gamma}_f^y = \hat{\gamma}_{f,\,\mathrm{old}}^y (1 - p_{ft})^{-1/2} \tag{80a}$$

and

$$\hat{\gamma}_b^y = \hat{\gamma}_{b,\,\mathrm{old}}^y (1 - p_{ft})^{1/2} \tag{80b}$$

it can easily be shown that both bc's for forward and backward particles at $y = 1 + \Delta y/2$ are satisfied exactly. The θ fluxes, $\hat{\gamma}_{f,b}^\theta$, may be adjusted, but there is no necessity, since both $\partial/\partial y(\hat{\gamma}_{f,b}^y) = 0$ and $\partial/\partial\theta(\hat{\gamma}_{f,b}^\theta) = 0$, making y fluxes and θ fluxes decoupled with regard to the divergence condition. The proposed adjustment of $\hat{\gamma}_{f,b}^y$ can also be shown to make the bc's at the detrapping side exactly satisfied.

The p_{ft}, appearing in Eq. (80), is still defined in terms of the ratio of the y fluxes at either side of the $y = 1$ boundary, formally as in Eq. (31). Since the

[redacted]

$\hat{\gamma}_t^y(y = 1^-)/\hat{\gamma}_f^y(y = 1^+) \equiv \hat{\gamma}_{t,\,\mathrm{old}}^y[1 - (p_{ft})_{\mathrm{new}}]^{1/2}/\hat{\gamma}_{f,\,\mathrm{old}}^y(y = 1^+) \equiv [1 - (p_{ft})_{\mathrm{new}}]^{1/2}$ $(p_{ft})_{\mathrm{old}}$. Or, with $(p_{ft})_{\mathrm{new}} \equiv x$, the unknown, and $(p_{ft})_{\mathrm{old}} \equiv a$, a constant readily evaluated from the ratio of the two "old" y fluxes at $y = 1^+$ and $y = 1^-$, the quadratic equation to be solved is $x^2 + a^2 x - a^2 = 0$. Since the "old" y fluxes in FPSTEL are θ independent, the evaluation of a and x at one poloidal mesh point suffices.

Figure 6 shows the result of incorporating the $(1 - p_{ft})^{1/2}$ factors in the y fluxes. Figure 6a is the contour plot of the backward distribution function obtained with FPSTEL. In Fig. 6b, we show the result of the y-flux adjustment. Both cases are for the $\nu^{1/2}$ regime.

Further careful consideration of this issue suggests that the $(1 - p_{ft})^{1/2}$ factors are in fact only needed for blocked particles, i.e., those that can reach the $y = 1$ boundary. This measure would, however, violate the divergence condition, since it would make the y flux y dependent, taking a jump near $y_{tp} = y_{tp}(\theta)$. Since these corrections are small, we presume that their influence on the fluxes for $y > y_{tp}$ is negligible.

These adjustments of the flows for $y > 1$ discussed in the context of FPSTEL are also used in the code FLOCS, albeit with some minor modifications. One of the main differences is that in FLOCS the θ and y fluxes, $\hat{\gamma}_{n>}^\theta$ and $\hat{\gamma}_>^y$, are generalized and each have non-zero derivatives, in contrast to Eq. (26), which holds for FPSTEL.

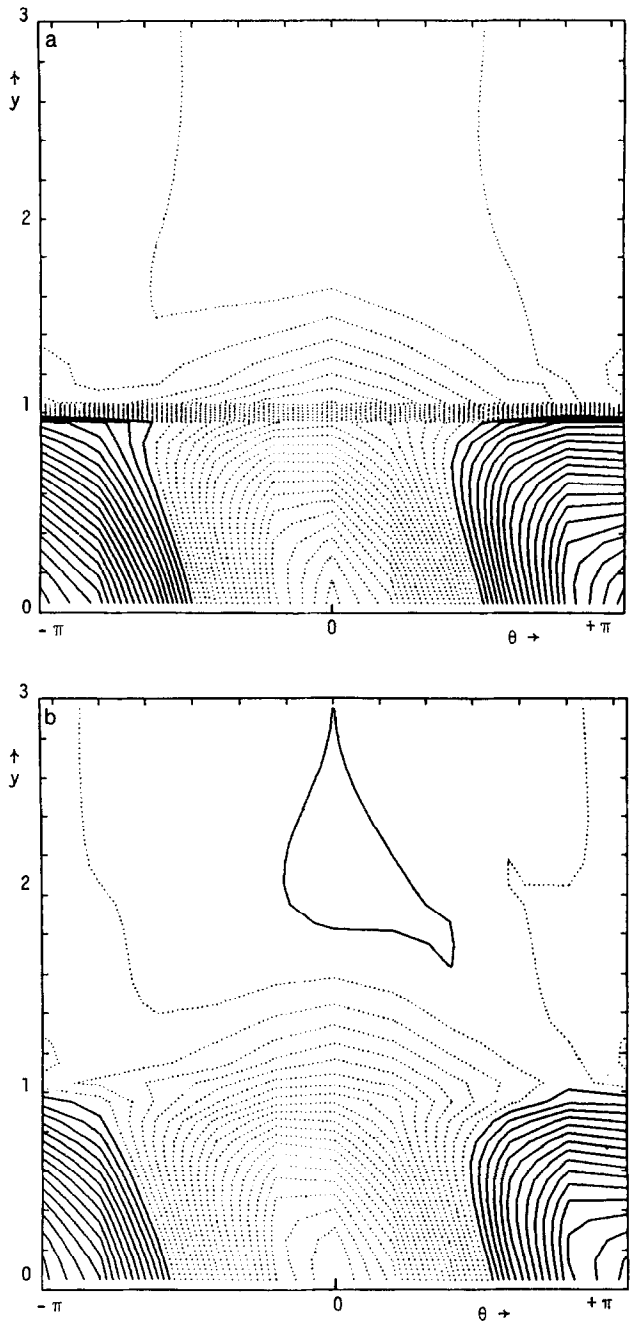

FIG. 6. (a) Contour plot of the *backward* ION distribution function in the $\nu^{1/2}$ regime, obtained with FPSTEL. (b) Contour plot of the *backward* ION distribution function in the $\nu^{1/2}$ regime, after the forward and backward flows were adjusted according to Eq. (80).

Amongst other things, one of the consequences is that $D_\theta \hat{\gamma}^\theta_{f,b}$ no longer vanishes in the equations above. More importantly, the divergence condition now requires that any adjustment that is made to one of the fluxes $\hat{\gamma}^y_>$ or $\hat{\gamma}^\theta_{n>}$ is compensated by an adequate adjustment of the other flux, $\hat{\gamma}^\theta_{n>}$ or $\hat{\gamma}^y_>$, respectively.

In contract to FPSTEL, the trapping probability p_{ft} is now slightly θ dependent because of the θ dependence of μ in $\hat{\gamma}^y_>$, Eq. (59b). This complicates matters if we merely use adjustments $(1-p_{ft}(\theta))^{1/2}$ in the y and θ fluxes, in that the θ dependence of p_{ft} causes the divergence condition to be violated. Therefore, we compromise by using the θ averaged trapping probability $p_{ft,\,\mathrm{av}}$ in the adjustment factor rather than the actual $p_{ft}(\theta)$. The error made in the divergence condition at $y=1$ is of the order of the difference $p_{ft}(\theta)-p_{ft,\,\mathrm{av}}$, which is very small.

In the standard version of FLOCS, we adjust the $\hat{\gamma}^y_>$ and $\hat{\gamma}^\theta_{n>}$ fluxes similarly:

$$\begin{aligned} \hat{\gamma}^y_f &= \hat{\gamma}^y_{f,\,\mathrm{old}}(1-p_{ft,\,\mathrm{av}})^{-1/2}, \qquad & \hat{\gamma}^\theta_f &= \hat{\gamma}^\theta_{f,\,\mathrm{old}}(1-p_{ft,\,\mathrm{av}})^{-1/2} \\ \hat{\gamma}^y_b &= \hat{\gamma}^y_{b,\,\mathrm{old}}(1-p_{ft,\,\mathrm{av}})^{1/2}, \qquad & \hat{\gamma}^\theta_b &= \hat{\gamma}^\theta_{b,\,\mathrm{old}}(1-p_{ft,\,\mathrm{av}})^{1/2}. \end{aligned} \tag{81}$$

The "old" fluxes are given in Eq. (59), where forward is given by a + sign and backward by a − sign.

In the FLOCS framework, the p_{ft}'s appearing in the quadratic equation are θ dependent: now $a \equiv a(\theta)$ is evaluated at every poloidal mesh point *ip*, after which $x \equiv x(\theta)$ is found. Then, $\bar{x} = \sum_{ip}^{npol} x(ip)/npol \equiv p_{ft,\,\mathrm{av}}$ is taken as the average trapping probability and is substituted for p_{ft} in Eq. (80), to give Eq. (81).

In Fig. 7 we show a comparison between the two possibilities for FLOCS concerning this issue. We show contour plots of the backward distribution function, $\langle f_b \rangle$, for ions in the transition region $v - v^{1/2}$. For Fig. 7a, Eqs. (81) were used. The divergence condition is satisfied everywhere except exactly at the $y=1$ boundary where there is a very small imbalance. In Fig. 7b, the $p_{ft,\,\mathrm{av}}$ in Eq. (81) has been replaced by $p_{ft}(\theta)$. Here the boundary condition at $y=1$ is satisfied exactly, but the divergence condition is spoiled for the whole region $y>1$. The first option seems to give the best results, but the difference is negligible.

e. *Structure of the Code FLOCS*

To discuss the structure of the code FLOCS it is useful to write the kinetic equation explicitly for a species, e.g., for untrapped ions,

$$\begin{aligned} &\frac{\partial \langle f^i \rangle}{\partial t} + \frac{1}{\langle J \rangle}\left\{\frac{\partial}{\partial \theta}(\langle J \rangle \langle \dot{\theta} \rangle_> \langle f^i \rangle) + \frac{\partial}{\partial y}(\langle J \rangle \dot{y}_> \langle f^i \rangle)\right\} + \langle \dot{r} \rangle f'_M \\ &\quad = \frac{1}{2}(\nu_\perp^{i/i} + \nu_\perp^{i/e}) \langle L(\langle f^i \rangle) \rangle \\ &\qquad + \{(\nu_\perp^{i/i} + \nu_\perp^{i/e})/2 - (\nu_s^{i/i} + \nu_s^{i/e})\} \frac{\langle v_\parallel \rangle}{v^2} \langle u_i(v) \rangle f^i_M \\ &\qquad + 2 \frac{\langle v_\parallel \rangle}{v_{Ti}^2} (\nu_s^{i/i} \langle r_{ii} \rangle + \nu_s^{i/e} \langle r_{ei} \rangle) f^i_M, \end{aligned} \tag{82}$$

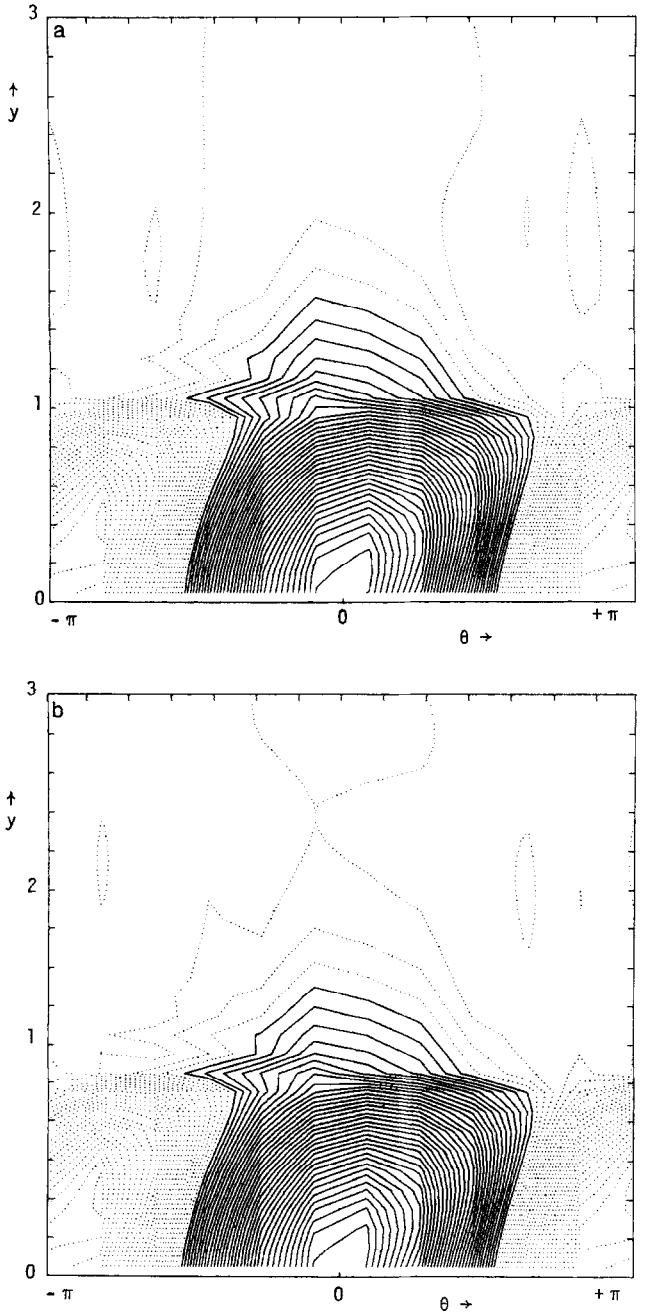

FIG. 7. (a) Contour plot of the *backward* ION distribution function with correction factors $(1 - p_{ft,\,\mathrm{av}})^{1/2}$ in the phase-space flows. (b) Contour plot of the *backward* ION distribution function with correction factors $(1 - p_{ft}(\theta))^{1/2}$ in the phase-space flows.

where

$$\langle u_i(v)\rangle f_M^i \equiv \frac{3}{4\pi}\int d\Omega \langle v_{||}\rangle \langle f^i\rangle \tag{83a}$$

$$\langle r_{ei}\rangle \propto \int d^3v\, m_e v_s^{e/i} \langle v_{||}\rangle \langle f^e\rangle. \tag{83b}$$

The complete collision operator has been given in Refs. [26, 5]. We repeat that $C_i(f^i) = C_{ii}(f^i, f^i) + C_{ie}(f^i, f^e)$. The symbol L in Eq. (82) stands for the y derivative part of the Lorentz collision operator. (Recall that the momentum-restoring terms, Eq. (83), do not appear in the $y < 1$ equation).

The finite-difference equivalent at a generic point (iy, ip) is given in Eq. (74). The timestep Δt is chosen. The fluxes $\hat{\gamma}_n^\theta \equiv \langle J\rangle\langle\dot{\theta}\rangle$ and $\hat{\gamma}_n^y \equiv \langle J\rangle \dot{y}$ and the Jacobian $\langle J\rangle$ are obtained from Eqs. (59) and (37) for $y > 1$. For $y < 1$, the flows listed in Eqs. (15), (20), (11)–(13) and the Jacobian given in Eq. (17) apply. For $y > 1$, again, the $\langle\dot{r}\rangle$ of the driving term is written in Eq. (44) and the Lorentz part of the collision operator in Eq. (49). For $y < 1$, the usual FPSTEL forms, Eqs. (11), (12), and (30), hold.

At the upper point of a mesh, Eq. (75) instead of Eq. (74) is to be used, where now Eq. (76) is employed rather than Eq. (59a). The other quantities are as in the generic case.

For the boundary conditions at the very top of the last mesh, the procedure is outlined above Eqs. (77), (78). For the boundary $y = 1$, the generic form, Eq. (74) holds, except that the term within the curly brackets is replaced by Eq. (79), in which one should read $\hat{\gamma}(iy, ip)\langle f(iy, ip)\rangle$, wherever a $\hat{\gamma}$ appears (in other words, Eq. (79) was written for $f \equiv 1$).

p_{fl}'s is given below Eqs. (80) and (81).

The electron distribution function, $\langle f^e\rangle$, influences the distribution function for ions, $\langle f^i\rangle$, via the r momentum-restoring term of the collision operator. Similarly, $\langle f^i\rangle$ enters the equation for $\langle f^e\rangle$. The r collision term represents collisional friction between the species.

A second observation is that energy scattering is absent from Eq. (82). Hence, Eq. (82) can be solved on a given energy shell. However, to find r_{ab}, Eq. (83b), integrations over energy must be performed.

The electric field appears in the code as a parameter. It enters the equation for $y < 1$ in the $\langle\dot{\theta}\rangle$ term. First a search for the self-consistent electric field E_r must be undertaken: that E_r for which ion and electron radial fluxes are equal. As we explained above, this search can be performed with a fairly low maximum y value, $y_{\max} \sim 3$, allowing the total run time for one value of E_r to be reduced by a factor ~ 5. (Also, because the radial fluxes are mainly determined by the ripple-trapped particles, no momentum-restoring terms are used for that run.)

The code is two-dimensional in the variables (θ, y). It computes $\langle f\rangle =$

$\langle f(\theta, y)\rangle$. To find the energy dependence, the code sequentially and iteratively handles different kinetic energies K_j, for each species (allowing for interspecies interaction), all within a single run.

Since $\langle f^b\rangle$ enters the equation for $\langle f^a\rangle$, the problem is solved iteratively. We start the code for one species, say ions. For the first iteration the r term is neglected, so that the coupling between species is not taken into account the first time through. In this first iteration, we run the code for ions for, say 10 kinetic energy values: e.g., $K_1 = 0.4T$ to $K_{10} = 4T$. For each of these K_j, the function $[\langle f^i(\theta, y)\rangle]_1$ is computed and stored in an output file. After $[\langle f^i\rangle]_1$ has been computed for the last kinetic energy for ions, the code switches to electrons and runs through 10 kinetic energies for electrons, e.g., $K_1 = 0.8T$ to $K_{10} = 8T$. (The reason for considering the electrons up to $K = 8T$ compared to the ions, for which we take $K \leqslant 4T$, is related to the fact that the electrons are in the ν^{-1} regime, whereas ions find themselves in the ν–$\nu^{1/2}$ regimes. A detailed scaling analysis addressing this issue has been undertaken in Ref. [12]). Again, for each of these K_j, $[\langle f^e(\theta, y)\rangle]_1$ is stored in an output file for $\langle f\rangle$. At the end of the first iteration, $[\langle f^i\rangle]_1$ and $[\langle f^e\rangle]_1$ are available, allowing the integrals $[\langle r_{ii}\rangle]_1$, $[\langle r_{ie}\rangle]_1$, $[\langle r_{ei}\rangle]_1$, and $[\langle r_{ee}\rangle]_1$ to be performed. These energy integrations are performed during cycling through the energies.

With the $[\langle r_{ab}\rangle]_1$ known, we start the second iteration. We read the $[\langle f^i\rangle]_1$ from disk and use that as the initial $\langle f^i\rangle$ for the second iteration which finds the distribution function, $[\langle f^i\rangle]_2$, in which $[\langle r_{ii}\rangle]_1$ and $[\langle r_{ei}\rangle]_1$ are used. We again cycle through all the ion kinetic energies, compute $[\langle f^i\rangle]_2$, $[\langle r_{ii}\rangle]_2$ and $[\langle r_{ie}\rangle]_2$. Then we switch to electrons and use $[\langle r_{ee}\rangle]_1$ and $[\langle r_{ie}\rangle]_1$ in order to compute $[\langle f^e\rangle]_2$. From this $[\langle f^e\rangle]_2$, $[\langle r_{ee}\rangle]_2$, and $[\langle r_{ei}\rangle]_2$ are computed.

For the results presented in the next section, we used 10 iterations as described above. In other words, the r collision terms are neglected during 10% of the run, and are then iterated on.

In the code, $\langle f\rangle$ is normalized to 1, i.e., $f_M = 1$, except when the energy integrals are performed, when obviously the $e^{-K/T}$ dependence is taken into account. At the start of the run, $\langle f\rangle$ is set to 1 (thus $\langle f_1\rangle = 0$). The driving term $\langle \dot{r}\rangle f'_M$ produces a $\langle \Delta f\rangle$, which is then felt by the $\partial/\partial y$ and $\partial/\partial\theta$ terms and the Lorentz collision operator. After a time $T \sim 1/\nu$, $\partial\langle f\rangle/\partial t$ becomes negligible, signaling that a steady state has been reached.

To speed up the code, $\langle f\rangle$ is only set equal to 1 for the first kinetic energy cycled through (for both ions and electrons). Rather than starting with $\langle f\rangle = 1$ for $K = K_j$, during the first iteration, we use the output $[\langle f\rangle]_1$ from the energy $K = K_{j-1}$. The behavior of $\langle f\rangle$ for two neighboring energies (i.e., collision frequencies) is not too drastically different; hence we reach equilibrium quite quickly. Obviously, this borrowing of the computed $\langle f\rangle$ from $K = K_{j-1}$ to start up the $\langle f\rangle$ for $K = K_j$ only makes sense during the first iteration. From the second iteration on, we start up the run for $[\langle f\rangle]_{k,K_j}$ with the old result for that same kinetic energy $[\langle f\rangle]_{k-1,K_j}$. In its present form, FLOCS uses about 1 h of CRAY CPU time for completing a full run, in which the starting distribution is a Maxwellian.

When a run has finished for a given set of plasma and device parameters, the result for $\langle f \rangle$ is saved in an output file. When the code is later run for a device with parameters which are not too different, the code can be started up using the $\langle f \rangle$'s of the old run rather than starting over from the beginning with $\langle f \rangle = 1$. This saves a considerable amount of CPU time (up to 60–70%).

VI. Results Obtained from FLOCS

In this section we report on some results obtained with the code FLOCS. In this paper, we discuss the distribution function and show the (θ, y) contour plots for ions and electrons. The determination of the self-consistent radial electric field for different plasma temperatures, the particle-confinement times and the radial particle fluxes, corresponding to these ambipolar fields, have been reported and discussed elsewhere [12]. Results for the bootstrap current and their physical interpretation, for two different ripple-amplitudes ε_h, have been considered in Ref. [25].

The device and plasma parameters investigated refer to an upscaled ATF-like reactor. (ATF is the Advanced Toroidal Facility located at ORNL). The parameters are given in Table I.

The series of plots shown in Figs. 8–17 depicts the contours of constant $\langle f_f \rangle$ (left) and $\langle f_b \rangle$ (right) in the (θ, y) plane for $0 \leqslant y < 3$. (For the region $y < 1$, $\langle f_f \rangle \equiv \langle f_b \rangle \equiv \langle f_t \rangle$.) They apply to the parameters of Table I. The set of the first five figures, Figs. 8–12, are for ions, the remainder, Figs. 13–17, are for electrons. For ions, five of the 10 kinetic-energy shells are shown: $K = 0.4T$, $1.2T$, $2.0T$, $2.8T$, and $3.6T$. For electrons, we also show five shells, from $K = 0.8T$ to $K = 7.2T$.

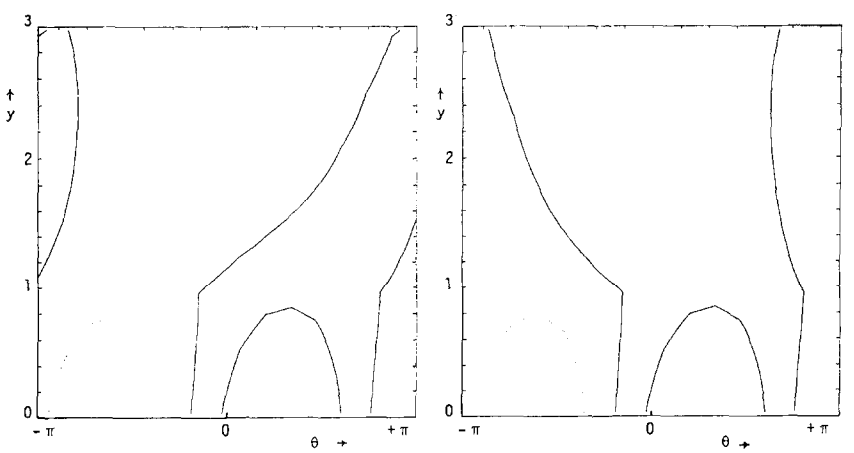

FIG. 8. Contour plot of *forward* (left) and *backward* (right) ION distribution functions for $K = 0.4T$. Distribution plotted every 0.5%.

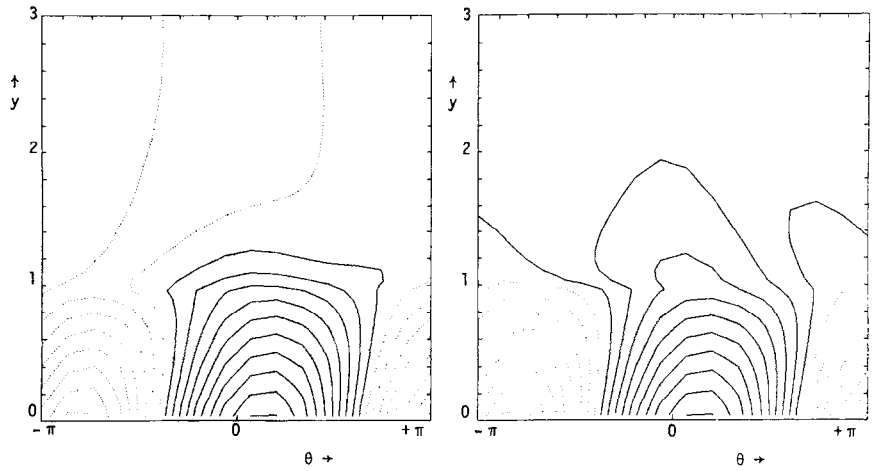

FIG. 9. Contour plot of *forward* (left) and *backward* (right) ION distribution functions for $K = 1.2T$. Distribution plotted every 0.5%.

In these contour plots, the computed distribution functions are represented normalized to $f_M \equiv 1$. The solid lines are contours of constant $\langle f \rangle$, for which $\langle f \rangle \geq 1$; $\langle f \rangle < 1$ is depicted by dotted curves. The range $0 \leq y < 3$ encompasses all ripple-trapped particles ($y < 1$), all toroidally blocked particles ($y < y_{tp}$), and some passing particles. y_{tp} is maximal at $\theta = 0$ with value 1.79. All the pictures, from Fig. 8 through 17, are plotted on the same scale. The interval, $0.8 \leq \langle f \rangle \leq 1.2$ is sampled 80 times. In other words, a constant $\langle f \rangle$ contour is plotted every time $\langle f \rangle$ changes by 0.5%.

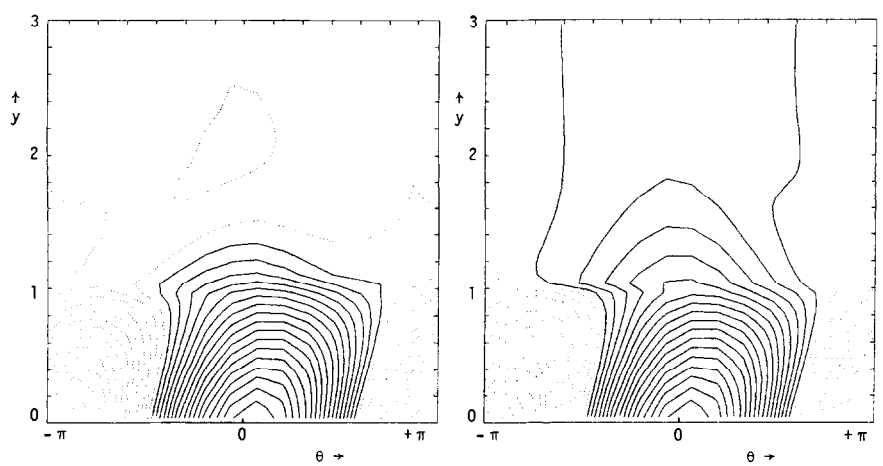

FIG. 10. Contour plot of *forward* (left) and *backward* (right) ION distribution functions for $K = 2.0T$. Distribution plotted every 0.5%.

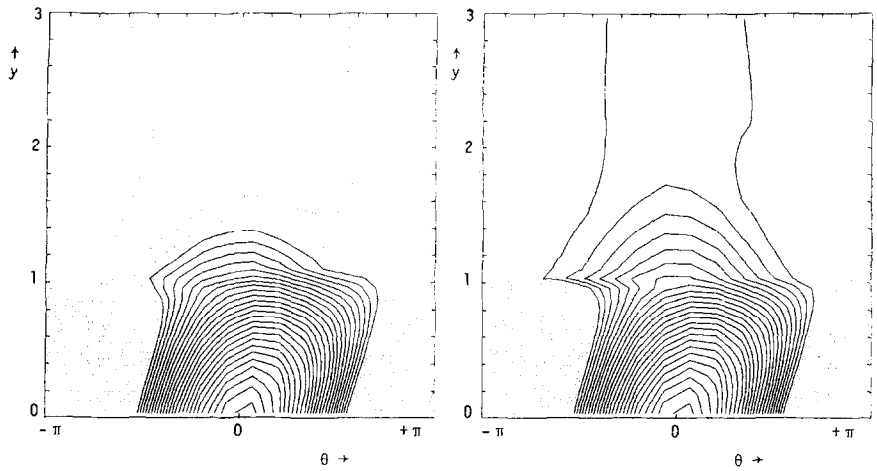

FIG. 11. Contour plot of *forward* (left) and *backward* (right) ION distribution functions for $K = 2.8T$. Distribution plotted every 0.5%.

The driving term of the kinetic equation is $\langle \dot{r} \rangle f'_M \equiv -\langle \dot{r} \rangle f_M / L_a$, in which L_a is the scale length. In FLOCS, the proper energy dependence of L_a is taken into account [12]:

$$L_a^{-1}(K) = -\left[\frac{p'}{p} + \frac{q_a \Phi'}{T} + \left(\frac{K}{T} - \frac{5}{2}\right)\left(\frac{T'}{T}\right)\right]. \tag{84}$$

The primes represent derivatives with respect to r. The presence of the $q_a\Phi'/T$ in L_a gives rise to a substantial difference between driving terms for ions and electrons.

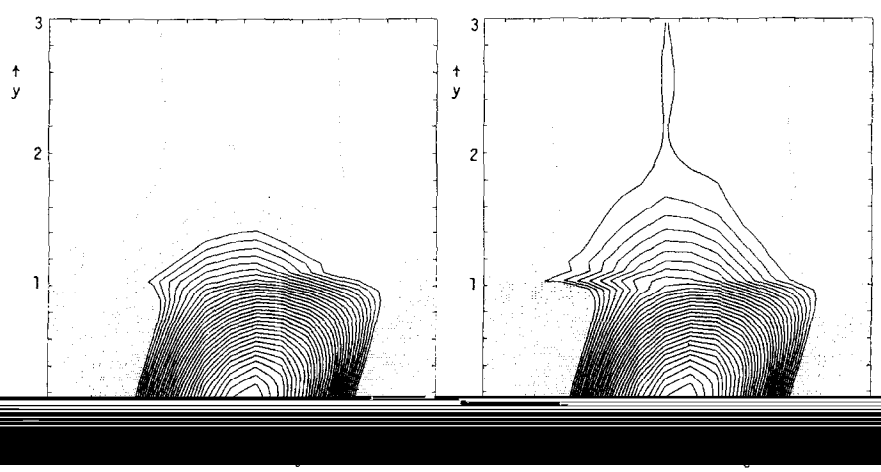

FIG. 12. Contour plot of *forward* (left) and *backward* (right) ION distribution functions for $K = 3.6T$. Distribution plotted every 0.5%.

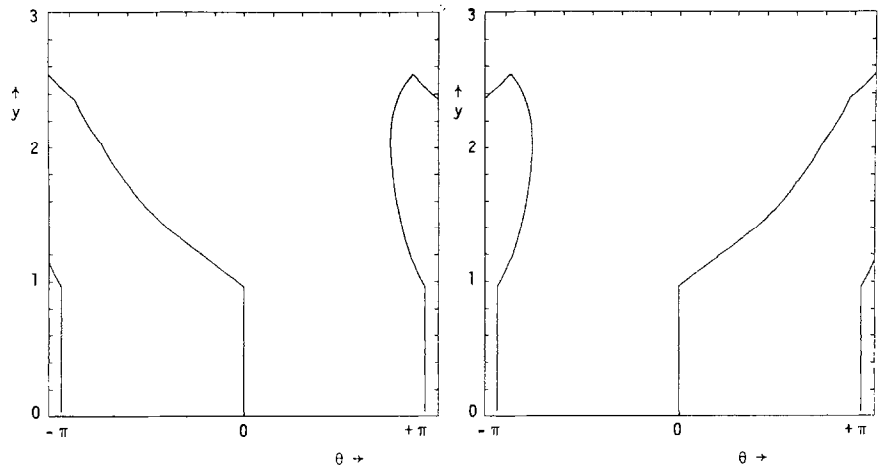

FIG. 13. Contour plot of *forward* (left) and *backward* (right) ELECTRON distribution functions for $K = 0.8T$. Distribution plotted every 0.5%.

It turns out that for the parameters used, the ambipolar electric field is negative, implying a positive Φ'. Consequently, the driving term for electrons is much bigger (L_a is much smaller) than the driving term for ions (which have a fairly large scale length). The parameters α_n and α_T of Table I are defined as $n'/n \equiv -\alpha_n/a$ and $T'/T \equiv -\alpha_T/a$, where a is the minor radius. These parameters α_n and α_T can be chosen at will in the code to simulate different radial profiles. As shown in Table I, we chose a nearly flat temperature profile. This was done in part for pragmatic reasons, to suppress the energy dependence of L_a, in order to be able to limit the

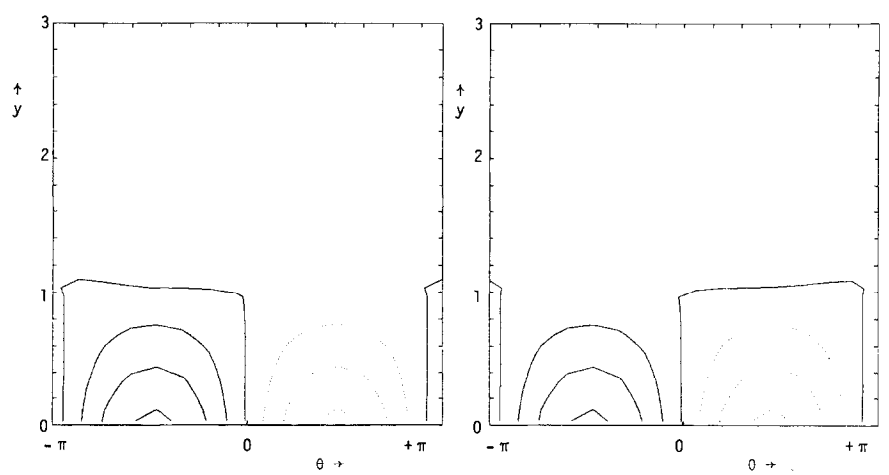

FIG. 14. Contour plot of *forward* (left) and *backward* (right) ELECTRON distribution functions for $K = 2.4T$. Distribution plotted every 0.5%.

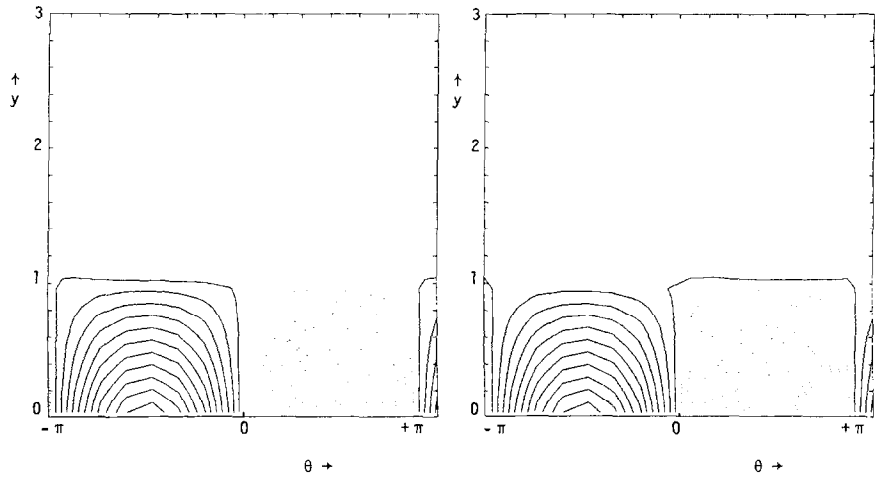

FIG. 15. Contour plot of *forward* (left) and *backward* (right) ELECTRON distribution functions for $K = 4.0T$. Distribution plotted every 0.5%.

range of energy integrations, and hence to save CPU time. This is also justifiable on physical grounds since stellarators usually have fairly flat temperature profiles. For the parameters in Table I, the ion and electron driving terms differ by roughly a factor 5.

We shall now briefly discuss these ion and electron distribution functions. First, we focus on the ions, Figs. 8–12. Next, the electrons, Figs. 13–17, are considered.

The ion distribution functions show that $\langle f \rangle$ shifts smoothly from the v^{-1} regime (low K) down to the v regime (large K) after having passed through the $v^{1/2}$

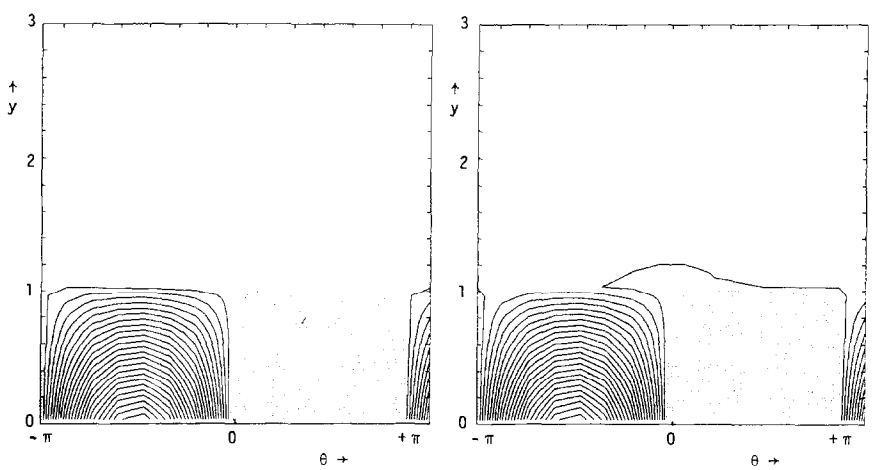

FIG. 16. Contour plot of *forward* (left) and *backward* (right) ELECTRON distribution functions for $K = 5.6T$. Distribution plotted every 0.5%.

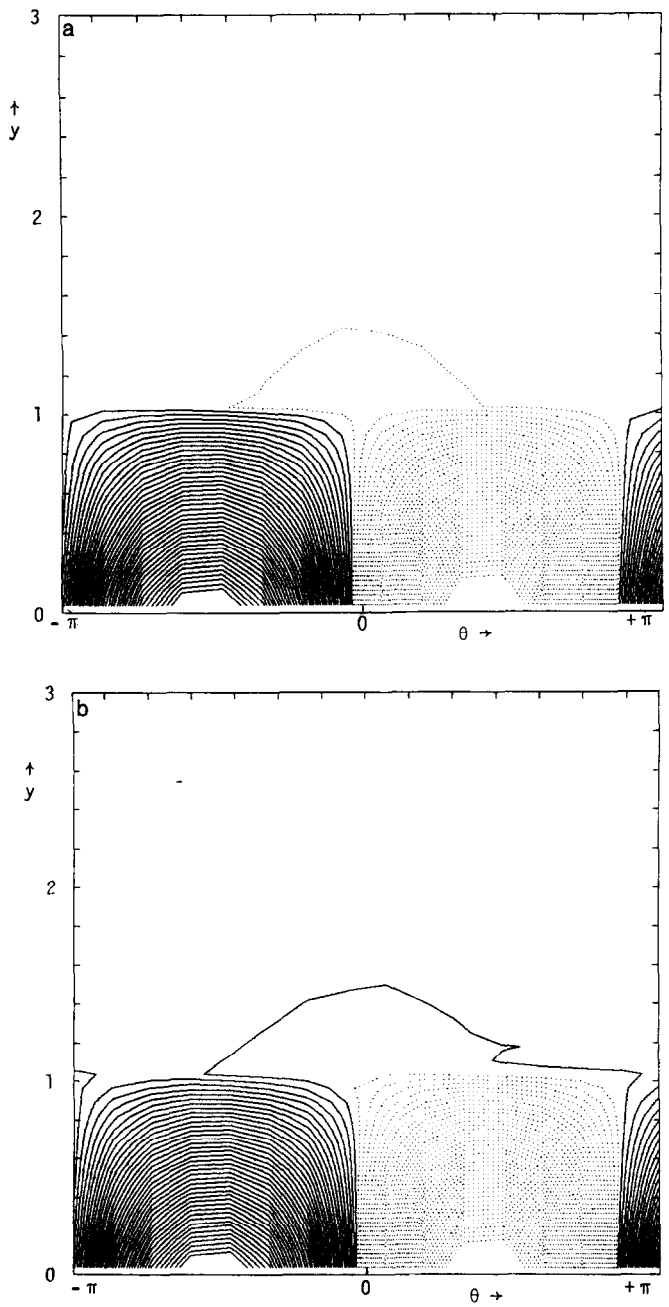

FIG. 17. (a) Contour plot of the *forward* ELECTRON distribution function for $K = 7.2T$. Distribution plotted every 0.5%. (b) Contour plot of the *backward* ELECTRON distribution function for $K = 7.2T$. Distribution plotted every 0.5%.

regime. In terms of the normalized frequency of Fig. 3, the low kinetic energy, $K=0.4T$, corresponds to $\nu_h/\Omega_E \sim 1.3$, whereas the large energy, $K=4.0T$, has $\nu_h/\Omega_E \sim 0.07$. In the relatively high collision-frequency regime, ν^{-1}, $\langle f_{1t} \rangle$ varies as $\sin\theta$. By lowering the collision frequency, the solid lines ($\langle f \rangle < 1$) move towards the middle of the picture, to make the θ dependence more and more symmetric. In the ν regime, $\langle f_{1t} \rangle$ varies roughly as $\cos\theta$.

The series of pictures, Figs. 8–12, shows more contours the less collisional the energy shell is. This is because, first, the driving term is proportional to $\langle \dot{r} \rangle$ which in turn varies linearly with K and, second, because collisions tend to restore f towards a Maxwellian, keeping the perturbation f_1 fairly small in the ν^{-1} regime.

The contours for $y>1$ for the relatively collisionless cases (Figs. 11, 12) resemble the collisionless particle trajectories. (See Refs. [3, 4].) This is because of Liouville's theorem; in the absence of collisions, f is constant along a phase-space trajectory. (For more on the behavior of $\langle f \rangle$ in the ν regime, see Ref. [3].)

The electron distribution functions shown in Figs. 13–17 are all in the ν^{-1} regime. Figure 13 refers to $K=0.8T$, or $\nu_h/\Omega_E \sim 70$; Fig. 17 depicts $\langle f \rangle$ for the case $K=7.2T$. $K=8T$ would correspond to $\nu_h/\Omega_E \sim 4$; ν_h/Ω_E for electrons does not scale exactly as $K^{-3/2}$ in comparison with the ions due to the energy dependence of the Maxwell integral ψ in the collision frequencies [9].

If we compare $\langle f \rangle$ for $y<1$ with that for $y>1$ in the case of electrons, we observe that $\langle f \rangle$ exceeds our window $0.8 \leqslant \langle f \rangle \leqslant 1.2$ near $y=0$ in Fig. 17, whereas those figures and all the other electron figures hardly show any detail for $y>1$ on this same scale. This can be understood from the kinetic equations, Eqs. (7) and (8). The large driving term for the electron species is relatively more

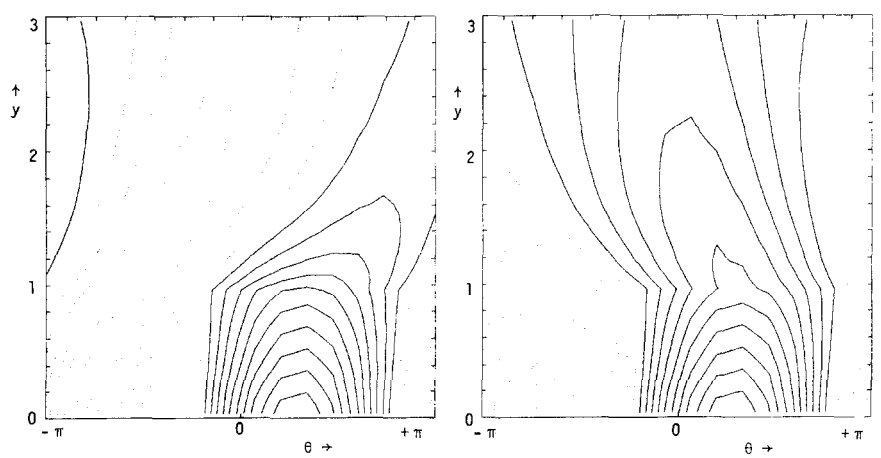

FIG. 18. Contour plot for *forward* (left) and backward (right) ION distribution functions of $K=0.4T$. Distribution plotted every 0.1%. Compare to Fig. 8.

important in the bounce-averaged equation for $y < 1$ than in the averaged equation for blocked particles because of the large phase-space flows $\langle \dot{\theta} \rangle$ and $\dot{y}$ for $y > 1$. Compared to the ions, $\langle \dot{\theta} \rangle$ and $\dot{y}$ are the same for the $y < 1$ equation, with the electrons having the biggest driving term. But for $y > 1$, the $\langle \dot{\theta} \rangle$ and $\dot{y}$ flows for electrons are a factor 43 larger than for ions.

To see some more structure for the region $y > 1$, we have replotted these same distribution functions on a five times finer scale. Now $\langle f \rangle = \text{const}$ contours are plotted for every 0.1% change in $\langle f \rangle$. Figure 18 is the finer scale equivalent of

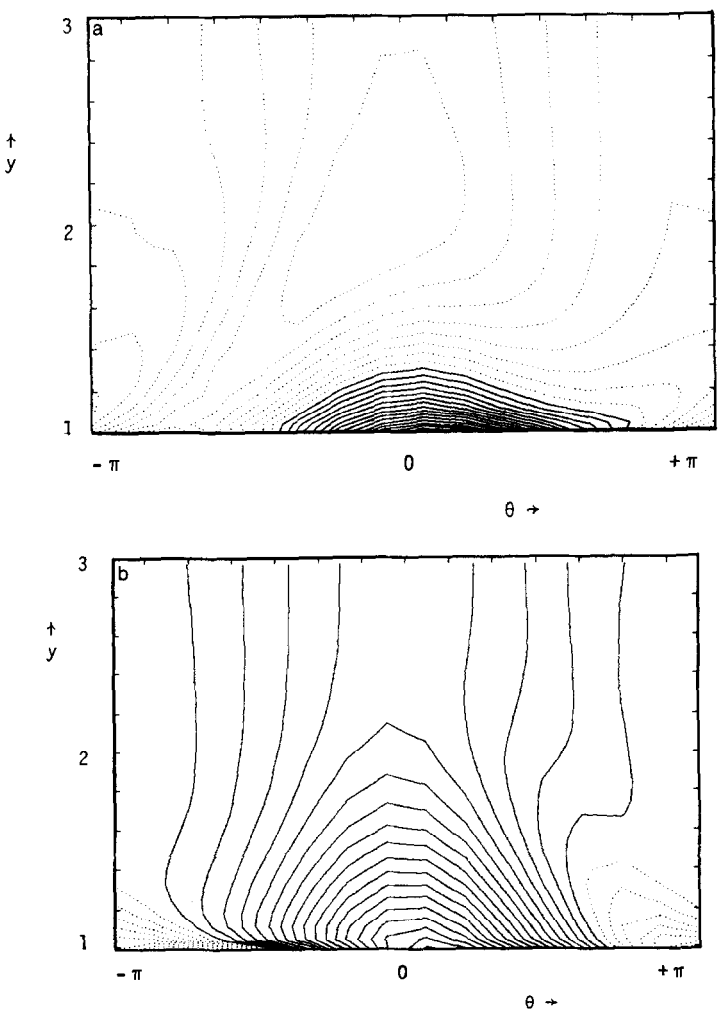

FIG. 19. (a) Contour plot of the *forward* ION distribution function ($y > 1$) for $K = 1.6T$. Distribution plotted every 0.1%. Compare to Fig. 20 for $y > 1$. (b) Contour plot of the *backward* ION distribution function ($y > 1$) for $K = 1.6T$. Distribution plotted every 0.1 %. Compare to Fig. 20 for $y > 1$.

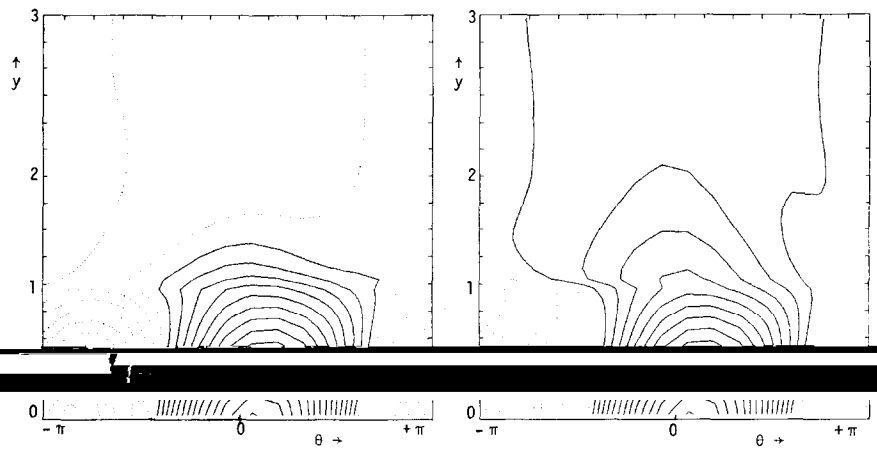

FIG. 20. Contour plot of *forward* (left) and *backward* (right) ION distribution functions for $K = 1.6T$. Distribution plotted every 0.5%.

Fig. 8 and refers to ions in the v^{-1} region (and $v^{-1} - v^{1/2}$ transition). In Fig. 19, we show the $y > 1$ region for ions with $K = 1.6T$; it should be compared with Fig. 20. Figure 21 shows the $y > 1$ portion of the forward distribution for electrons for $K = 7.2T$, which goes with Fig. 17.

From all the pictures given so far it is clear that $\langle f \rangle$ tries to be symmetric in θ for large y values regardless of its behavior in the ripple-trapped region. This is particularly noticeable in the pictures which have $\langle f_t \rangle$ in the $1/v$ regime. For $y < 1$, $\langle f_t \rangle \sim \sin\theta$ and for $y \gg 1$, $\langle f_t \rangle \sim \cos\theta$. See Figs. 18 and 19 for ions, and Fig. 21 for electrons. The symmetry for $y \gg 1$ comes about due to the large free-streaming phase-space flows $\langle \dot{\theta} \rangle$ and $\dot{y}$ for blocked and passing particles.

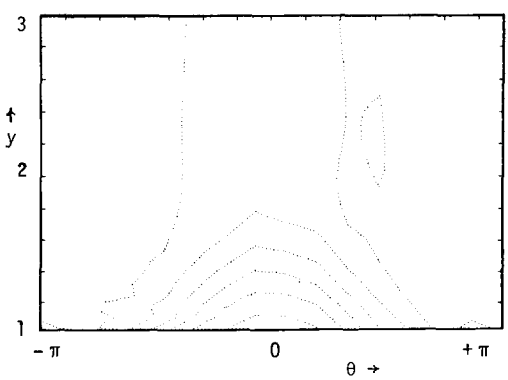

FIG. 21. Contour plot of the *forward* ELECTRON distribution function ($y > 1$) for $K = 7.2T$. Distribution plotted every 0.1%. Compare to Fig. 17.

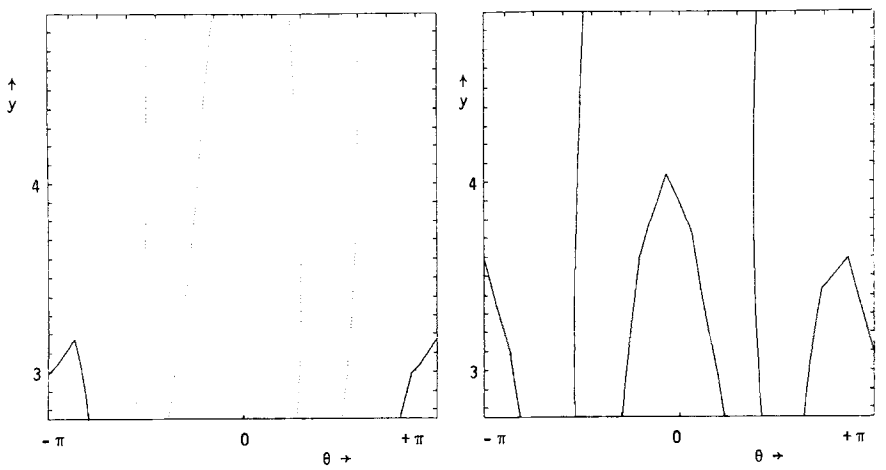

FIG. 22. Contour plots of the second mesh of *forward* (left) and *backward* (right) ION distribution functions for $K = 0.4T$. Distribution plotted every 0.1%. Compare to Fig. 18.

The higher-order meshes in y do not exhibit much structure to the eye. They show basically vertically oriented contours, roughly symmetric in θ. As an example, in Fig. 22, the second mesh, from $y = 3$ to $y = 5$, to be connected onto the first mesh of Fig. 18 is shown.

VII. SUMMARY AND CONCLUSIONS

We have developed what could be called a "two-and-a-half" dimensional numerical code, FLOCS, to compute the ba distribution function in stellarators, and thus to compute interesting variables such as radial fluxes, the self-consistent ambipolar radial electric field, parallel fluid flows, and parallel currents. It extends the range of validity of the 2D Fokker–Planck code, FPSTEL [3, 4], a code designed to compute radial particle fluxes of a single species with given energy. The designation $2\frac{1}{2}$ reflects the fact that the code itself is 2D, in (y, θ), but incorporates the important dependences on a third variable, the energy E.

An importance feature of FLOCS is that it is not limited to ripple-trapped particles; toroidally blocked and passing particles are also treated with sufficient accuracy. In addition, the full collision operator, including momentum-restoring terms, has been employed. Therefore, FLOCS can compute parallel currents. FLOCS deals with the "entire" velocity range, up to $y \simeq 100$. To accommodate such large y values, a multi-mesh numerical procedure was devised.

From the contour plots presented in Section VI, it can be concluded that most of the structure in $\langle f \rangle$ is confined to the region $y < 3$. However, it is the shift in $\langle f \rangle$ (i.e., the asymmetry between forward and backward particles) for large y values that is responsible for the parallel flows and current.

ACKNOWLEDGMENTS

The authors thank Dr. C. D. Beidler for useful discussions. This work has been supported by the Department of Energy Grants DE-FG02-87ER53201 and DE-FG02-87ER53216.A004.

REFERENCES

1. S. P. HIRSHMAN, *Phys. Fluids* **21**, 224 (1978).
2. K. C. SHAING AND J. D. CALLEN, *Phys. Fluids* **26**, 3315 (1983).
3. H. E. MYNICK AND W. N. G. HITCHON, *Nucl. Fusion* **26**, 425 (1986).
4. W. N. G. HITCHON AND H. E. MYNICK, *J. Plasma Phys.* **37**, 383 (1987).
5. L. M. KOVRIZHNYKH, *Nucl. Fusion* **24**, 851 (1984).
6. C. D. BEIDLER, Ph. D. thesis, University of Wisconsin-Madison, Torsatron/Stellarator Report TSL-87-7, December 1987 (unpublished).
7. W. N. G. HITCHON, *Nucl. Fusion* **22**, 1661 (1982).
8. W. N. G. HITCHON, K. D. MCLENITHAN, AND H. E. MYNICK, *Nucl. Fusion* **23**, 1143 (1983).
9. D. L. BOOK, *NRL Plasma Formulary*, Naval Research Laboratory, Washington, DC 20375, 1983 (unpublished).
10. H. E. MYNICK, *Phys. Fluids* **26**, 2609 (1983).
11. C. D. BEIDLER, W. N. G. HITCHON, W. I. VAN RIJ, S. P. HIRSHMAN, AND J. L. SHOHET, *Phys. Rev. Lett.* **58**, 1745 (1987).
12. W. D. D'HAESELEER, W. N. G. HITCHON, AND J. L. SHOHET, *J. Plasma Phys.* **42**, 133 (1989).
13. S. P. HIRSHMAN, *Nucl. Fusion* **18**, 917 (1978).
14. S. P. HIRSHMAN AND D. J. SIGMAR, *Nucl. Fusion* **21**, 1079 (1981).
15. M. CORONADO-GALLARDO, Doctoral thesis, Technische Universität München, July 1984 (unpublished). [German]
16. M. CORONADO AND H. WOBIG, *Phys. Fluids* **29**, 527 (1986).
17. M. CORONADO AND H. WOBIG, *Phys. Fluids* **30**, 3171 (1987).
18. K. C. SHAING, S. P. HIRSHMAN, AND J. D. CALLEN, *Phys. Fluids* **29**, 521 (1986).
19. E. RODRIGUEZ-SOLANO RIBEIRO AND K. C. SHAING, *Phys. Fluids* **30**, 462 (1987).
20. K. C. SHAING, S. P. HIRSHMAN, AND J. S. TOLLIVER, *Phys. Fluids* **29**, 2548 (1986).
21. T. OHKAWA AND M. S. CHU, General Atomic Report GA-A18688, November 1986.
22. Y. T. LAU, *Phys. Fluids* **30**, 3517 (1987).
23. S. P. HIRSHMAN, K. C. SHAING, W. I. VAN RIJ, C. I. BEASLEY, JR., AND E. C. CRUME, JR., *Phys. Fluids* **29**, 2951 (1986).
24. S. P. HIRSHMAN, K. C. SHAING, AND W. I. VAN RIJ, *Phys. Rev. Lett.* **56**, 1697 (1986).
25. W. D. D'HAESELEER, W. N. G. HITCHON, C. D. BEIDLER, AND J. L. SHOHET, *J. Plasma Phys.* (1991), in press.
26. S. P. HIRSHMAN, D. J. SIGMAR, AND J. F. CLARKE, *Phys. Fluids* **19**, 656 (1976); for a rigorous derivation see S. P. HIRSHMAN AND D. J. SIGMAR, *Phys. Fluids* **19**, 1532 (1976).